November 2011

THE UNIVERSITY OF WESTERN AUSTRALIA
Achieve International Excellence

Plasmonic Excitations in Nanostructures

(Thesis for Bachelor of Science with Honours)

Nikita Kostylev*

School of Physics, University of Western Australia

*Email: kostyn01@student.uwa.edu.au

Supervisors

Prof. Sergey Samarin

W/Prof. James Williams

Abstract

Keywords: surface plasmons, thin films, silver, gold, permalloy ($Ni_{80}Fe_{20}$), nanostructures, nanostripes, SPEELS, ellipsometry, Transverse MOKE.

Surface-plasmon-mediated confinement of optical fields might hold the key for on-chip miniaturization of future all-optical circuits [Temnov, 2010]. Realisation of such devices would predominantly rely on development of techniques of observation and custom tailoring plasmonic resonance effects to control electronic, magnetic and photonic properties of materials.

In this project we studied plasmonic excitations on a number of different types of nano-structures: continuous thin silver films on Si and W(110) and nano-patterned nonmagnetic and magnetic layers on silicon substrate. In the first case we used ellipsometry and reflection spectroscopy to optically observe plasmonic excitations in Ag/Si films. Spin-polarized electron energy loss spectroscopy (SPEELS) was used to compare the results with plasmon energy losses in ultra-thin Ag films prepared in-situ on W(110) substrate. Loss functions calculated on the basis of optical measurements were found to reproduce some of the energy loss features obtained from SPEELS.

Unique macroscopic samples in the form of 1D dense periodic arrays of gold and Permalloy ($Ni_{80}Fe_{20}$) nanostripes manufactured using DUV lithography allowed application of standard wide beam ellipsometry and reflection spectroscopy analysis to this type of nanostructure for the first time. Diffraction coupling of light to localized Surface Plasmon Polariton (SPP) modes has been observed in this system. A novel custom-made attachment was added to the ellipsometer setup that allowed us to record magnetic field-resolved spectra of the plasmon resonances. The Permalloy nanostripe geometry has been found to enhance the amplitude of the Transverse MOKE effect at plasmon-polariton resonant wavelengths. This phenomenon was explained by a shift of the SPP resonance frequency upon magnetisation reversal. Angle-resolved measurements of samples with different periods of stripes have shown angular-spectral and geometry tunability of the resonant processes. This suggests a viable method of controlling magneto-optical properties of the structure.

Table of Contents

Acknowledgements

I would like to express my sincere appreciation towards all those who gave me the possibility to complete this project.

First and foremost, I would like to thank my supervisors, Prof. Sergey Samarin and W/Prof. Jim Williams for all the invaluable help and support they have given me throughout this tough year. Thanks to Prof. Mikhail Kostylev for helping me stay on the right track during this project and not get lost in the huge quantities of accumulated data.

I am also deeply grateful to Paul Guagliardo for his assistance in teaching me how to operate the ellipsometer. A special thankyou goes to Prof. Vladimir Petrov and Peter Wilkie for all their help, in particular with perfecting the design of the electromagnets.

I would also like to express my gratitude as well as the gratefulness of my supervisors to our international colleagues. In particular, we wish to thank A/Prof. Adekunle Adeyeye from the National University of Singapore for letting us use the unique periodic nanostructured samples and taking time to manufacture the reference single-layer gold nanostripe array specifically for this work on a very short notice. For his generous contributions to the theoretical discussions, I would also like to acknowledge Prof. Andre Stashkevich, University Paris 13, France.

I. Introduction

General trends in electronic devices are minituarization, high speed of operation and data transmission, while consuming extremely low quantities of power. It has been suggested, however, that the performance of conventional semiconductor-based electronic circuits is becoming the limiting factor in the transmission of digital signals [Ozbay, 2006].

It is widely acknowledged that quantum gates and computers based on photonics and optical devices could potentially supersede current silicon-based semiconductor electronics [Peruzzo et al., 2011; Knill, 2010; Ross and Oskin, 2008]. Optical interconnects, such as fibre optic cables, are capable of carrying digital data with a capacity of more than 1000 times that of electronic interconnects [Ozbay, 2006]. Current developments in optical fibre technologies however, represent a major constraint, when it comes to integrating the technology into nanoscale-sized circuits. To this date, fibre optical interfaces and cables themselves are only scalable down to micrometre sizes, with the smallest implementations being ~1000 times larger than their electronic analogues [Ozbay, 2006].

Recent theoretical and experimental studies are looking at the possibility of circumventing the use of fibre optical interconnects in nanoscale-sized circuits altogether. One such proposal is to take advantage of surface plasmon excitations, which are electromagnetic waves that propagate along the surface of a conductor. Plasmonic circuits offer the potential to carry optical signals and currents in the same nanoscale metallic circuitry, thereby making it possible to combine the superior technical advantages of photonics and electronics on the same chip [Ozbay, 2006].

Effective integration of plasmonic circuitry within nanoscale devices requires the capacity to control electromagnetic radiation and its transmission at this minute level. An important step in developing this ability is to observe and study plasmon resonances in nanometre-thick films of different materials. Continuous improvements in the nanofabrication and nanocharacterisation capabilities [Temnov, 2010], have led to a rapid growth in the field of plasmonics, especially in the area concerned with plasmon excitations in metallic nanometric heterostructures. These perforated metal-dielectic substrate materials not only support surface plasmon polariton (SPP) modes but also allow one tuning their characteristics by changing the geometric parameters of the systems.

Magneto-optical (MO) effects (variations in polarization and intensity of scattered light that occur when magnetisation of material is reversed), are also of prime interest to photonic control, as they allow fast modulation of light polarisation and intensity via external magnetic fields [Prasad, 2004]. The main difficulty with MO effects is that their intensity is usually not high enough to be utilized in practical photonic systems [Belotelov et al., 2009].

In view of the above, this project was set to investigate characteristics of plasmon excitations in various types of nanostructures and relations between these characteristics and parameters of the systems. This project was undertaken with the following aims:

1. Fabrication of continuous thin films of metals with thicknesses lying in the nanometre range and measurement of their optical properties using ellipsometry.

2. Investigation of plasmon excitations in thin films using Electron Energy Loss Spectroscopy (EELS).

3. Investigation of plasmon resonances in complex periodic noble-metal and ferromagnetic nanostructures using a variable angle spectroscopic ellipsometer (VASE).

4. Designing and implementing a system to extend capabilities of VASE to include optical spectroscopic magnetic-field-resolved (MFR) studies.

5. Studying magneto-plasmonic coupling in ferromagnetic nanostructures using the upgraded MFR VASE ellipsometer.

This report is structured as follows. First, a short introduction to the general theory of plasmons in thin film is offered along with a brief overview of the most recent works in plasmonics and magnetoplasmonics. A separate chapter is dedicated to describing experimental techniques used in this work along with the appropriate theoretical basis to understand their principles. In the next chapter (Chapter IV) the results of the experiments are presented together with a thorough theoretical analysis, starting with optical detection of plasmons in thin films of Ag, and SPEELS spectroscopy of the Ag/W(110) system. Next we discuss the excitation of surface plasmons in periodic nanostructures, namely on arrays of parallel nanostripes made of gold and Permalloy nanostripes. Finally, we present the main results of our study, which are concerned with the enhancement of magneto-optical effects due localisation of surface plasmons in the geometry of single and bi-layer metal nanostripe arrays. In the end a conclusion is given together with a brief outlook for future studies.

II. Overview: plasmonics and magnetoplasmonics

1. Plasmons in thin films of metals

Many of the fundamental electronic properties of the solid state can be successfully described by the analogy of single electrons moving in a periodic potential of crysal lattice. A somewhat different approach is to derive the properties of the solid state is to consider the plasma concept: the free electrons of a metal are treated as an electron liquid of high density [Raether, 1988]. This approach was further developed by Pines and Bohm in the 1950s [Pines and Bohm, 1952] in order to explain the phenomena of energy losses in fast electron scattering experiments (Ruthemann, 1948). They have shown that the long-range nature of the Coulomb interaction between the sea of valence electrons in metals yields collective volume plasma oscillations similar to the electron-density oscillations observed in electrical discharges in gases.

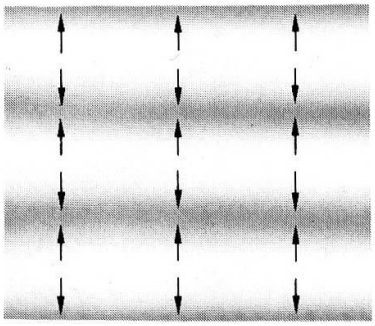

Figure II.1.1. Free longitudinal plasma oscillation. The arrows indicate the direction of displacement of the electrons. [Kittel,1986]

A *plasmon* is defined as a quantum of a plasma oscillation. In bulk of materials it can be excited at a frequency ω_p, for which the following condition is satisfied :

$$\varepsilon(\omega,0)=1-\frac{\omega_p{}^2}{\omega^2}, \quad \text{(II.1.2)}$$

where $\varepsilon(\omega,\vec{k})$ is the dielectric function of a crystal.

In general, *bulk plasmons* exist in materials at high energies and thus can only be excited by high energy electron scattering.

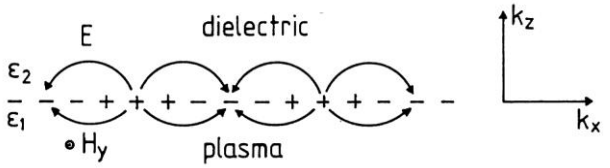

Figure II.1.2. Schematic representation of the charges and the electromagnetic field of SPs propagating in the *x*-direction. H_y shows the magnetic field in the *y*-direction of the *p*-polarized SP wave. [Raether, 1988]

Ritchie [1957] has shown that on boundaries, such as surface of materials, or thin films, a different type of plasmons can exist. These are the called *surface plasmons* or *surface plasmon-polaritons (SPPs)*. For the first time they have been experimentally observed here at UWA by electron scattering [Powell and Swan, 1959; Swan and Robins, 1960].

Surface plasmons propagating at the flat interface between a conductor and a dielectric are essentially two-dimensional electromagnetic waves, which exponentially decay with distance from both sides of the interface (Fig. II.1.2). These plasmons have lower energies than bulk plasmon resonances and in certain cases can be excited not only by electrons but by photons of the light.

In thin films the dispersion relation of surface plasmons is a complex function that depends on the properties of the material at the interface, namely the complex dielectic functions $\hat{\varepsilon} = \varepsilon' + i\varepsilon''$ of the metal (ε_1) and of the dielectric (ε_2). The frequency of surface plasmons can be derived from Maxwell's equations (a detailed derivation of these formulas can be found in Appendix A). It is given by:

$$\omega_{sp} = \frac{\omega_p}{\sqrt{1+\varepsilon_{II}}}, \qquad \text{(II.1.3)}$$

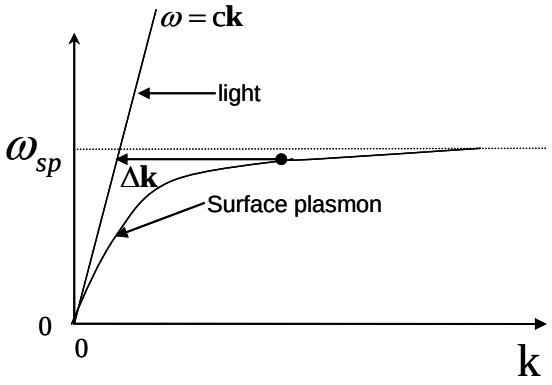

Figure II.1.3. Dispersion of a surface plasmon and light. Δk is an "extra" wave vector to match the wave vector of a photon (light).

where ε_I and ε_2 are the dielectric functions of metal and dielectric respectively. The requirement [Raether, 1988]

$$\varepsilon_{II}(\omega_{sp}) = -\varepsilon_{air} = -1 \qquad \text{(II.1.9)}$$

can be used as an indicator to test for plasmon excitation in thin films when the dielectric is air. Implicit in this resonant condition is the assumption that the imaginary part of the dielectric responce, ε_{II}', is much less than 1, so that the plasma oscillations are not heavily damped by one-electron excitations [Jasperson et al., 1969].

In general, surface plasmons can only be excited by p-polarized light (TM polarizon). This is dictated by the continuity conditions at the boundaries between two materials [Mayer, 2007]. Moreover, the surface plasmon dispersion curve (Fig. II.1.3) typically lies to the right of the light line for the dielectric (given by $\omega = ck$), which means that excitation by light is not possible unless special techniques to match the wave vector of light to the resonance are employed. This can be achieved, for example, by using prism coupling, a technique known as attenuated total reflection [Mayer, 2007]. In the Kretschmann configuration, two dielectrics on both sides of a film are used. A light beam is reflected at the interface between an insulator with a large dielectric constant, usually in the form of a prism, and the metal. This provides the light with sufficient momentum to excite surface plasmons at the interface between the metal and the lower-index dielectric, i.e. in this case at the metal/air interface.

2. Surface Plasmon-Polaritons in nanostructures

After a short spike of activity upon the discovery of surface plasmon-polaritons in the 1950-1960s, the research in this field has progressed at a rather slow rate. It wasn't until the breakthrough in nanotechnology

in the end of 1980s that the science of surface plasmons began to experience a rapid growth.

The 'second birth' of SPPs and the recent rapid development of research in the area occurred when it was found that surface plasmon modes in metallic structures of dimensions smaller than the wavelength of light may lead to the localisation of guided light signals far beyond the diffraction limit for electromagnetic waves in dielectric media [Gramotnev, et al., 2010]. This allows the beam to be concentrated into region as small as a few nanometres, limited only by the atomic structure of matter, dissipation and the spacial dispersion of light [Liebsch, 1985, Larkin et al., 2004]. As a consequence of the above findings, a large number of new designs of nanostructures have been proposed and studied that exploited the variety of optical effects that were previously considered impossible.

One of the most striking examples of phenomena linked to surface plasmons localised on the nanometric level is the phenomenon of extraordinary light transmission. It has been found that in apertures of nanometric proportions light can be transmitted through the sample without experiencing any diffraction [Ebbesen, 1998]. As it turned out, localised surface plasmons excited in this system by the incident light were responsible for reemission of the beam on the other side of the aperture (Fig. II.2.1).

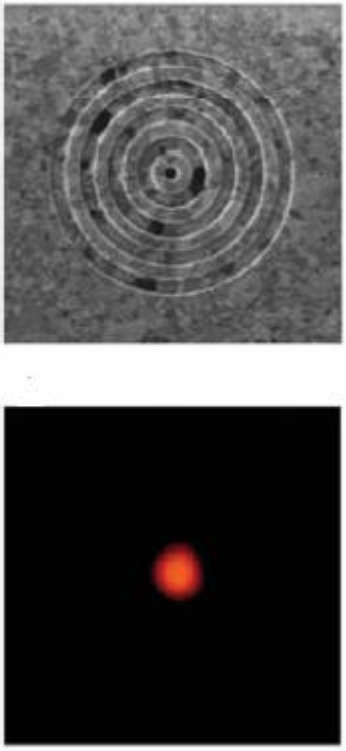

Figure II.2.1. Top: Focused ion beam image of a bull's eye structure surrounding a circular subwavelength aperture in a 300 nm thick silver film. **Bottom:** Optical image of the directional emission at the wavelength of peak transmission. [Maier, 2007]

Other important applications due to surface plasmons in nanostructures that have been recently reported include: creating a plasmonic blackbody (i.e. almost complete absorption of light) in gold nanogratings [Kravets, 2008], designing, fabricating and characterizing subwavelength waveguide components [Charbonneau, et al., 2000; Lamprecht et al., 2001; Nikolajsen, 2003], implementing plasmons as modulators and switches [Krasavin et al., 2004, Krasavin et al., 2005], and even acting as mediators in the transfer of energy from donor to acceptors molecules on opposite sides of metal films [Andrew and Barnes, 2004].

3. Magnetoplasmonic effects in nanostructures

The field of plasmonics studies the variety of all the optical phenomena that arise in nanostructured systems that exhibit surface plasmon resonances. A particularly intriguing branch of this field began to develop in the last 3-4 years, which is related to magneto-plasmonic coupling in nanostructures. This branch,

titled magnetoplasmonics, is concerned with developing ways to control the behaviour of surface plasmons under the influence of external magnetic fields by nanopatterning.

The latest discovery in the area of magnetoplasmonics in nanostructured materials is the enhancement of magneto-optical effects in these systems, such as the Faraday rotation, or polar Kerr rotation [Wurtz, et al., 2008]. The techniques of utilising plasmons in order to enhance magneto-optical effects have already been well-established for plain, multi-layer or granular films [e.g. Safarov et al., 1994]. However it has been recently found that the introduction of periodic patterns into films of specially-chosen metals results in much higher gains due to the localisation of surface plasmons.

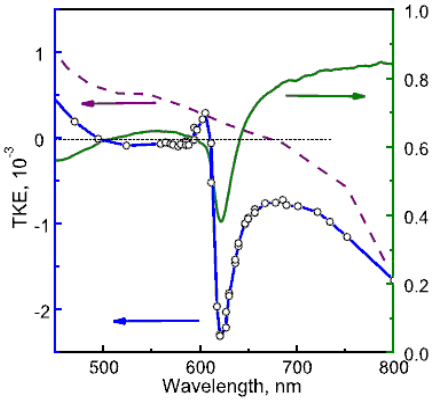

Fugure II.3.1. TMOKE of all-nickel grating with *d*=320nm, *h*=100, angle=68°. Dotted curve: TMOKE spectrum for a grating; solid curve: reflectivity spectrum; dashed: reference TMOKE of a plain nickel film. [Grunin, 2010].

In particular, it has been determined that plasmonic nanostructures have the ability to significantly enhance the Transverse Magneto-Optical Kerr Effect (MOKE), which leads to a change in intensity of reflected light (see discussion in section III.2 for details) [Belotelov et al., 2009]. This effect has been recently observed in all-nickel subwavelength nanogratings [Grunin et al., 2010]. For this structure fabricated entirely from a ferromagnetic metal, an enhancement of an order of magnitude has been established when compared with the weak TMOKE signal of a plain nickel film (see Fig. II.3.1).

The above findings seem to have started a race to develop even better nanomaterials, the ones that can be used to tailor the magneto-optical responses for particular needs. For example, Belotelov et al. [2011] showed how one could use gold slits on a ferromagnetic dielectric substrate to maximize the transverse MOKE gain by exploiting the lower light absorption characteristics of noble metals and small optical losses in the dielectric.

Characterisation of magneto-plasmonic effects in different types of materials, as well as geometries, is currently a hot topic as this could potentially result in such applications as developing the methods to control light propagation in plasmonic circuits.

III. Experimental techniques

1. Spectroscopic Ellipsometry

Ellipsometry is an optical technique that is concerned with analysis of surfaces and composition of thin films of materials. It is based on the measurement of variation of polarisation state of light that is reflected form a plane surface. The technique has been invented more than one hundred years ago, but it is only since the 1980's, with the advances in microelectronics and computer technology, that it became popular. Ellipsometry has now found a wide range of applications, from scientific research in chemistry and surface studies, to more applied fields, such as electronics and development of semiconductor devices.

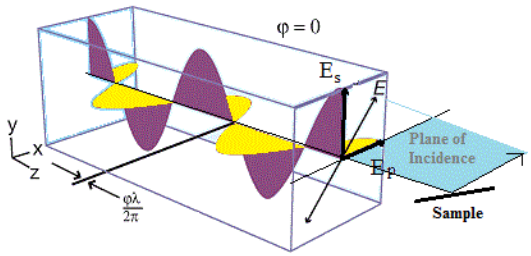

Figure III.1.1. Linearly polarized light incident on a sample. Amplitudes of *s*- and *p*-components of $\vec{E}$ are equal and the phase difference is zero.

After reflecting from a sample surface, a linearly polarized light beam (Fig. III.1.1) is generally elliptically polarized (Fig. III.1.2). This means that the amplitudes of *s*- and *p*-components of the electric field are altered, and so is the relative phase difference between them. The exact nature of the change in polarization is determined by the sample's properties, such as thickness, complex refractive index or its dielectric function.

Although optical techniques are inherently diffraction limited, ellipsometry only measures two parameters: ψ and Δ. The ψ-parameter is proportional to the ratio of amplitudes of $\overrightarrow{E_s}$ and $\overrightarrow{E_p}$, while Δ gives their phase difference. Since no absolute values are recorded, the sensitivity is greatly increased and can in principle reach angstrom resolution [VASE manual].

The ellipsometry values are directly related to the Fresnel (reflectance) coefficients r_p and r_s for *p*- and *s*-polarized light respectively:

$$\rho = \frac{r_p}{r_s} = \tan(\psi)e^{i\Delta} \quad , \qquad \text{(III.1.1)}$$

where ρ is known as the complex reflectance ratio.

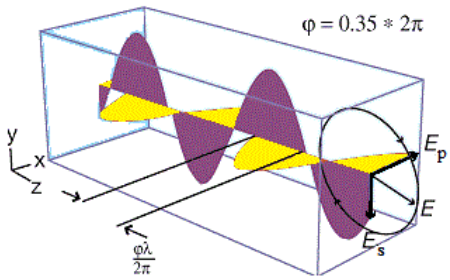

Figure III.1.2. Elliptically polarized light incident on a sample. Amplitudes of *s*- and *p*-components of $\vec{E}$ are not equal and the phase difference is arbitary.

Spectroscopic ellipsometry, the measurement of ellipsometric parameters over a range of wavelengths, is very sensitive to the film thickness. As the film thickness increases, there is an increasing separation between

the light reflected from the surface and the light that travels through the film, as shown in Fig. III.1.3. This causes a phase delay that is related to both the physical thickness and the index of refraction. This phase delay is usually different for different polarizations of light and thus directly affects the ellipsometric quantities. It is therefore possible to estimate the physical parameters of the sample by fitting a model constructed from optical measurements of reference films. As long as the materials comprising the sample are known, such parameters as film thickness and optical constants can be determined.

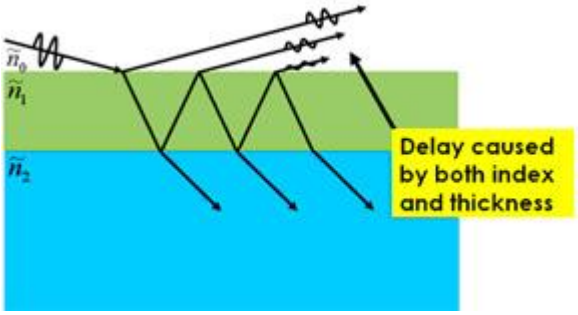

Figure III.1.3. Scattering of light from a sample media with refractive index n_i.

Data from Eqn. (III.1.1) can be directly used to estimate the so-called pseudo-dielectric constants of the sample material. They are found from:

$$\tilde{\varepsilon} = \varepsilon_1 + i\varepsilon_2 = \sin^2(\phi_i)\left[1+\left(\frac{1-\rho}{1+\rho}\right)^2 \tan^2(\phi_i)\right] \quad . \qquad \text{(III.1.2)}$$

The complex refractive index of the material can therefore be also found. It is related to the dielectric constant via the expression:

$$\tilde{\varepsilon} = (n+ik)^2 . \qquad \text{(III.1.3)}$$

The pseudo-dielectic function $\tilde{\varepsilon}$ should however be used with caution, since it assumes a perfectly flat substrate with infinite thickness [Fujiwara, 2009]. Surface roughness can also cause interference, which may affect the estimates.

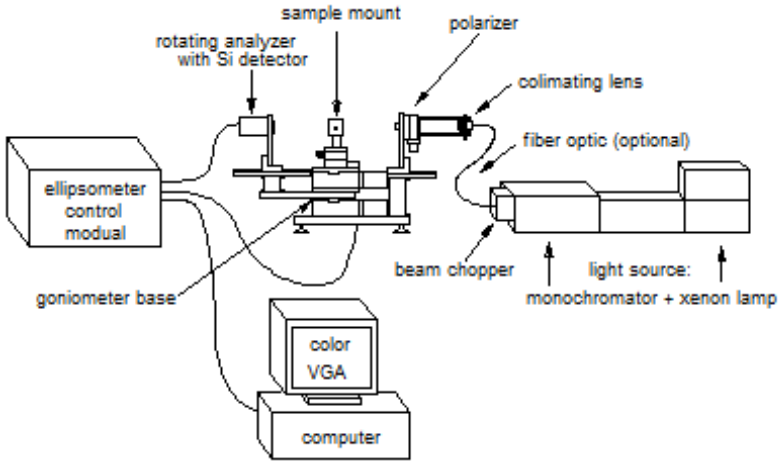

Image III.1.4 Schematic of the VASE ellipsometer setup.

Optical measurements discussed in this report have been conducted using a *variable angle spectroscopic ellipsometer (VASE)* manufactured by J.A. Woolam Co.[1] (see Fig. III.1.4). The ellipsometer utilizes a standard wide white beam (~ 4 mm in diameter), generated by a xenon light source. The beam is passed through a monochromator, which adjusts the wavelength to a required value, with a bandwidth of 3nm [VASE Manual]. The total range of operation is specified as λ = 200 - 1100 nm, corresponding to near-UV, visible, and IR region. Nevertheless, preliminary

[1]VASE® with Xenon Lamp, VB-200 electronics control module, ST-200 Translator Module, PC: Pentium III, 800MHz.

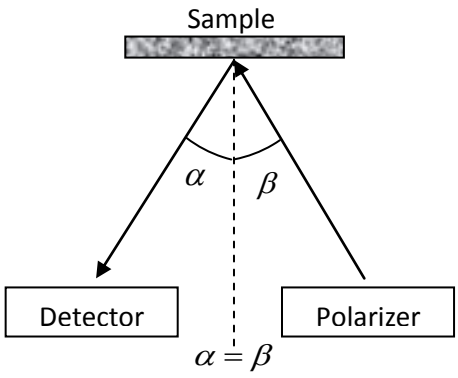

Figure III.1.5. Diagram of the measurement geometry of VASE.

tests have shown that the usable spectral range, over which the sampled data have an acceptable error, is slightly narrower, approximately 380-1050 nm.

The primary function of this device is measuring thicknesses of multi-layered thin film samples. Multi-layered films are rather complicated structures to characterize optically, since a lot of variables affect the dispersion and polarisation of light. The ellipsometer design has therefore been advanced to include a goniometer, which adjusts the angle of the sample surface relative to the beam. In the ellipsometric mode, the apparatus records the ψ and Δ parameters (using a rotating analyser with a solid state reflector) over a number of incident angles. This allows one to separate the contribution of the multiple layers to the polarization state of the reflected light, significantly improving the accuracy of the technique. It has to be noted here that due to calibration reasons VASE is limited to sample data only in the specular geometry (Fig. III.1.5).

The sample thickness is determined by using the modelling function incorporated into the VASE software. The software contains a database of refractive indexes for a number of dielectrics, metals, and semiconductors from which a model of the sample could be built. For optimal regression the software also requires to enter an initial guess for the layer thickness. The fitting is conducted automatically, with the algorithm selecting the required type of fits depending on chosen materials.

The VASE is a multi-functional device: besides recording the ellipsometric parameters, it is also capable of recording reflectance values over the spectral range of operation. Reflectance is given as the ratio of intensities of incident and reflected beams. It is related to the Fresnel coefficients via $R = rr^*$.

The direct control of the polarizer makes it possible to measure the absolute values of R separately for *s*- and *p*-polarized incident beams. This functional mode, together with the ability to adjust the angle of incidence, makes the device invaluable in characterizing the reflective properties of thin film structures. It is especially important for complex nanostructures, since the nature of resonance phenomena is likely to be revealed by comparison of reflectivity spectra of different polarizations.

2. Transverse Magneto-Optical Kerr Effect (TMOKE) and Magnetic Field-Resolved (MFR) Ellipsometry

Magneto-optical Kerr effects (MOKE) are the commonly used effects for characterising surface magnetism [Zvezdin et al., 1997]. They are also used for imaging domains and magnetic singularities. As compared to longitudinal and polar Kerr effects that exhibit a change of polarisation when the magnetisation of surface under examination is reversed, the transverse magneto-optical Kerr effect (TMOKE) has the advantage that light remains linearly polarised after reflection, under the condition that it is *p*-polarised and that the measured magnetisation component is parallel to the surface and perpendicular to the plane of incidence [Penfold, 2002].

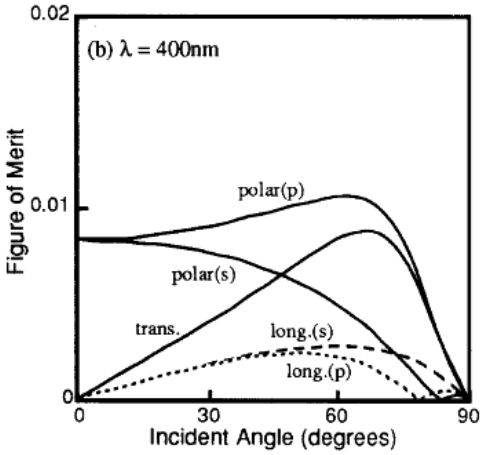

Figure III.2.1. Calculated figure of merit of different types of MOKE for a TbFeCo film. Figure of merit for TMOKE is directly related to R_p amplitudes.Image: [Kokogawa, 1993].

The magnetic effect represents a change in reflectivity of the surface. The amplitude reflection at a surface is formally described by the Fresnel coefficient matrix [r_{ij}]:

$$[r_{ij}] = \begin{bmatrix} r_{pp} & r_{sp} \\ r_{ps} & r_{ss} \end{bmatrix}. \qquad \text{(III.2.1)}$$

TMOKE is only concerned with r_{pp}. If an interface between air (or vacuum) and metal is considered, then r_{pp} can be calculated by starting with the Helmoltz equation and by taking into account the boundary conditions [Sokolov, 1967]. The final expression is composed of two parts, the usual (non-magnetic) Fresnel coefficient and the term induced by magnetism

$$r_{pp} = \left[\frac{N\cos(\theta_i) - \gamma}{N\cos(\theta_i) + \gamma} \right] + i \left[\frac{2m_x NQ\beta\cos(\theta_i)}{\left(N\cos(\theta_i) + \gamma\right)^2} \right] \qquad \text{(III.2.2)}$$

where $N = n + ik$ is the complex index of refraction, θ_i the angle of incidence, *Q* the complex magneto-optic coefficient, β - the unit vector along the refracted beam, γ - the gyro-magnetic ratio and $m_x = \frac{M_x}{M}$, the relative magnetisation component along *x*, i.e. perpendicular to the plane of incidence and parallel to the sample surface. The sign of the second term changes when magnetisation is reversed, since, for a uniaxially magnetised surface along *x*, m_x changes from +1 to -1. Consequently, the reversal of magnetisation will generally vary both the amplitude and the phase of the reflected light.

From Eqn. (III.2.2) it follows that to probe the transverse MOKE effect, all that is necessary, is to measure the reflectivity R_p and the variation of its phase relative to the *p*-polarized incident beam. Although this is possible with a different instrument – a high-sensitivity optical reflection setup, there are significant disadvantages in this approach with respect to using the VASE.

The graph of typical amplitudes of TMOKE for metals (see Fig. III.2.1) shows that the associated Kerr rotation causes a change in R_p of a factor of 0.01 or less, which is lower than the statistical error of reflectivity measurements by VASE (~0.025).

On the other hand, this particular ellipsometer has been already used to measure the polar MOKE effect [Heenan, 1998] in the ψ / Δ mode. It was therefore expected that the sensitivity of the ellipsometry detector was sufficient to detect the Kerr rotation. Since in TMOKE the only quantity that changes is $r_{pp} = r_p$, the measurement of variation in ψ would be proportional to the change in R_p. The Δ parameter would then provide us with the phase data.

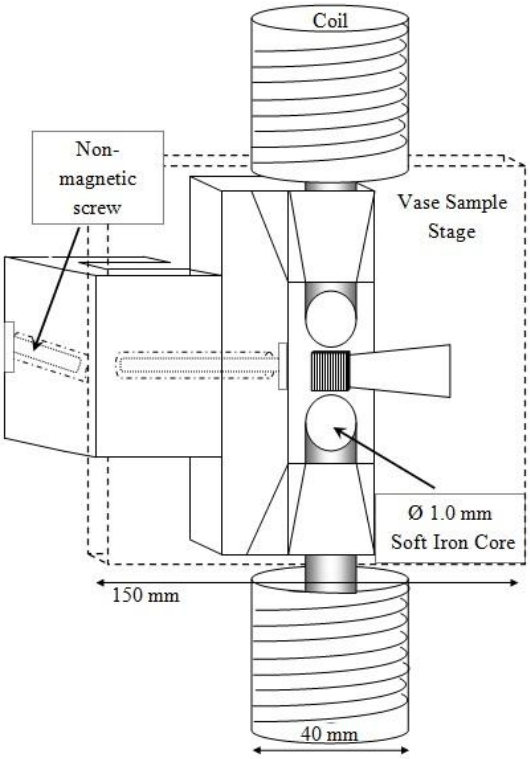

Figure III.2.2. Custom designed electromagnet attachment to VASE. Primary material: HDPE plastic. Soleinods are 350 turns of 0.75mm copper wire wound on a hollow plastic core of 13mm diameter. The iron cores are slided into the solenoids.

To induce the Magneto-Optical Kerr effect in ferromagnetic samples, a uniform uniaxial magnetic field $\vec{B}$ is required. The direction of the field and, preferably, its amplitude has to be adjustable, in order to directly observe the change in ψ / Δ values and to exclude the possibility of any contributions to the output signal unrelated to MOKE. An electromagnet with coil windings was therefore chosen as the most suitable source of $\vec{B}$: it satisfied all of the above requirements and was simple to construct. As a part of this Honours project, a suitable electromagnet has been designed and fabricated. The coils have been made from thick 0.75mm diameter insulated copper wire to reduce resistance to prevent overheating at high currents. The wire has been wound around a hollow PET plastic core. The magnetic field strength inside the solenoids was measured with a magnetometer to be 250 Oe.

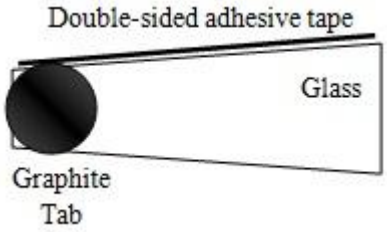

Figure III.2.3. Glass sample holder for the magnet.

Because of the time constraints, instead of rebuilding the whole sample stage of VASE, an attachment to the stage to hold the coils in place had been built (see Fig. III.2.2). The peculiarities of VASE's sample stage design meant that the coils had to be placed quite far away from the samples – approximately 7cm away. It was known from ferromagneric resonance measurements [Kostylev et al., 2010] that the level of magnetisation saturation of the samples under study was around 100-200 Oe. To achieve the required field strength and minimise overall weight of the attachment, soft iron cores had been incorporated into the design. They significantly increase the magnetic field by adding the stray field of the ferromagnetic cores to the magnetic field produced by the coils and concentrate all of the magnetic field in a small volume, just enough to place the sample. A sample holder for this application has also been made from a microscope glass slide cut in a form of a trapezoid (see Fig. III.2.3). The glass was attached to the sample stage with double sided sticky tape. The samples were affixed to the glass with adhesive graphite tabs.

It was of significant interest to conduct TMOKE measurements over the whole frequency range of the ellipsometer's spectrum, given that spectral positions of magneto-plasmonic effects, if there existed any, was not known *a priori*. A single sweep across the whole optical spectrum of VASE usually takes at least 30 minutes. This means that two consecutive measurements for opposite directions of $\vec{B}$ would take more than an hour. Since a sample is attached to the sample stage with low strength stretchable glue (sticky tape) and is hanging vertically, it would be apt to move slowly relative to beam. Parameter drift in electronics is also likely to be significant. With the sensitivity of the ellipsometer being just above the amplitude of the Kerr rotation, spectral measurements over long times would therefore be impossible.

An alternative to doing full optical spectrum sweeps for a set $\vec{B}$ would be to sweep the magnetic field separately for each wavelength of the dataset. Since recording a single spectral point takes no longer than 30 seconds, this would make the setup insensitive to long term drifts. It would also be much easier to accumulate reasonable statistics by averaging the effect at each λ by increasing the number of sweeps of $\vec{B}$.

Considering the large number of points in a full spectrum sweep (at least 100 for an appropriate resolution), the only effective way to sweep $\vec{B}$ was to use a computer controlled current supply. Unfortunately, all power supplies of this type available to the group were in active use for other research projects. The only device[2] that was vacant had an analogue control port. The current output of the supply was proportional to the input voltage (in the range ±10V). For computer control, a Digital-to-Analog (DAC) conversion card was therefore required. Instead of purchasing a universal DAC, it has been decided to design and manufacture a custom control module as a part of the present Honours project.

[2] Kepco BOP36-6M 10 Amp Bipolar Voltage/Current Supply

Figure III.2.4. Custom-designed external PC-controlled DAC card.

The DAC card has been constructed as an external control box (see Fig. III.2.4). An Arduino Mega 2560 16MHz microprocessor board was chosen as the digital controller. This board has a USB data port, which supports two-way communication with the PC via a virtual serial interface (COM port). It also has a large number of digital ports for communicating with different types of integrated circuits (IC).

All of the circuits have been based on manufacturers' datasheets. The separate board that contains the 4-channel 10 bit DAC converter IC and the corresponding voltage buffering/amplifying circuit has been designed and simulated using the PSPICE Computer-Aided-Design software. The principal diagram of the complete system and detailed schematics are given in Appendix B. Here only the circuit of a single DAC channel (Fig. III.2.5) will be discussed. On this example the concept of operation of the device can be easily understood.

The Arduino microprocessor board receives commands via USB or directly from the user (via a touchscreen). The microprocessor processes the commands, and instructs (via an I2C digital interface) the DAC IC to set its output voltage to the required level. Since the output of the IC ranges only from 0 to 4 V, and the input of the Kepco current supply requires a voltage of ±10V, the voltage has to be scaled and shifted.

The capacitor C1 filters out high-frequency noise of the DAC. The scaling and shifting is handled by a summing operational amplifier (op-amp). The output of this amplifier is given by the following equation:

$$V_{sum} = -(R_4 + R_a)\left(\frac{V_{DAC}}{R_3} + \frac{V_{SHIFT}}{R_3}\right), \qquad \text{(III.2.1)}$$

where V_{SHIFT} is the output of an inverting amplifier (all other values are explained in Fig. III.2.5). From this equation it can be seen that, assuming a constant V_{SHIFT}, the output of the DAC is scaled by $-(R_4 + R_a)/R_3$. The output is also shifted by the amount $-\left((R_4 + R_a)/R_3\right)V_{SHIFT}$. The value of V_{SHIFT} can be adjusted by varying R_s, according to the equation of the inverting amplifier:

$$V_{SHIFT} = -\frac{(R_2 + R_s)}{R_1}V_{REF}. \qquad \text{(III.2.2)}$$

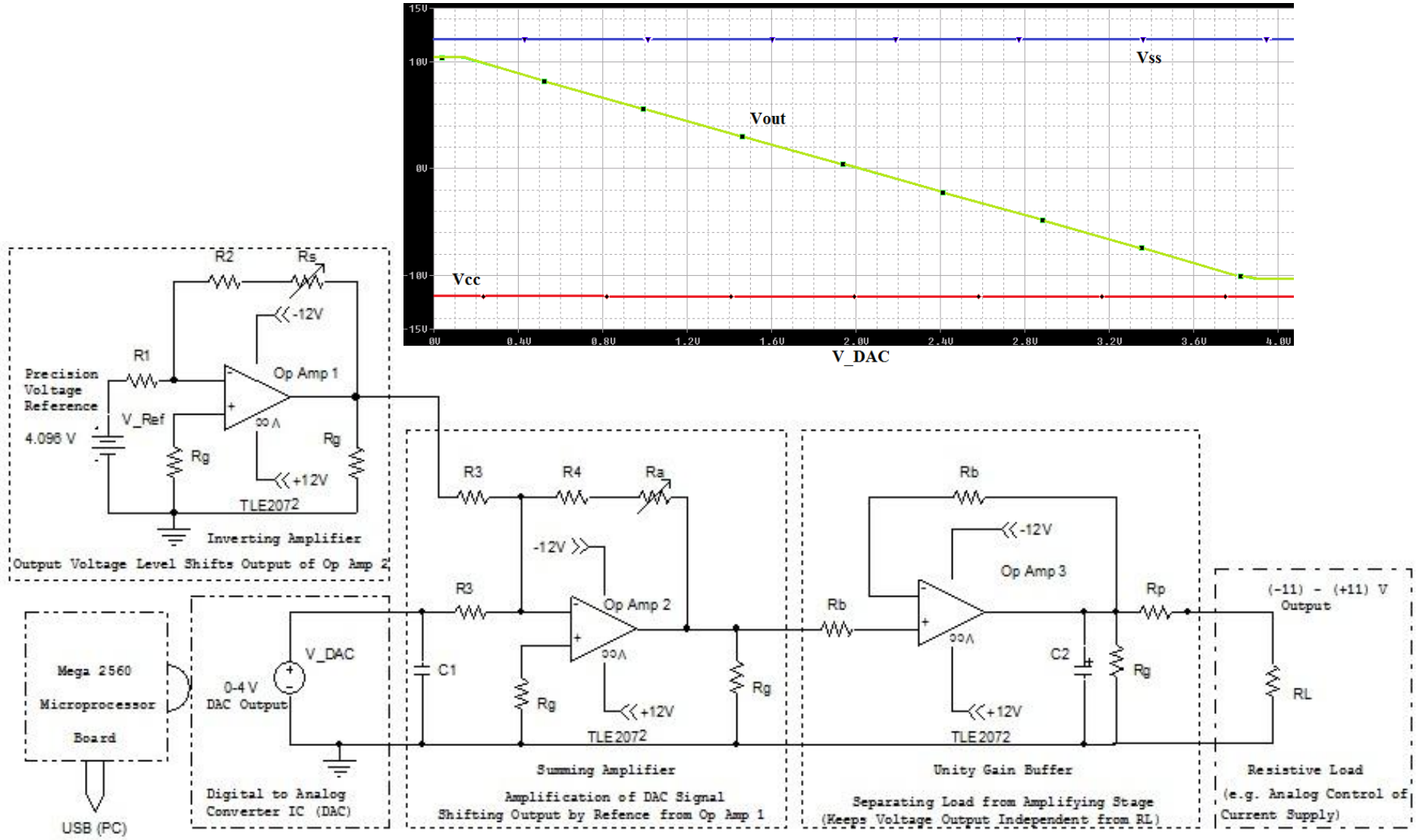

Figure III.2.5. Circuit diagram of one of the channels of the DAC board. See appendix B for more detail. **Inset (Top right): PSPICE similation of amplifer stage output.**

In order to minimize the fluctuations in V_{SHIFT}, the voltage V_{REF} is set by a high-precision voltage reference IC. Finally, the output of the summing amplifier is fed through a unity gain buffer. This allows to decouple the shifter/amplifier stage from the load resistance.

At the same time, the buffer amplifier can be chosen of arbitrary type. For example, a high power op-amp can be used to supply a high current to the output of the system. After adjusting the variable resistances R_a and R_s, the output voltage of the DAC looks like the one in the top inset of Fig. III.2.5.

After successfully constructing the DAC box, specialised custom software has been written (see Appendix C) that processes the output of the ellipsometer in real time and switches the direction of magnetic field $\vec{B}$ at required times.

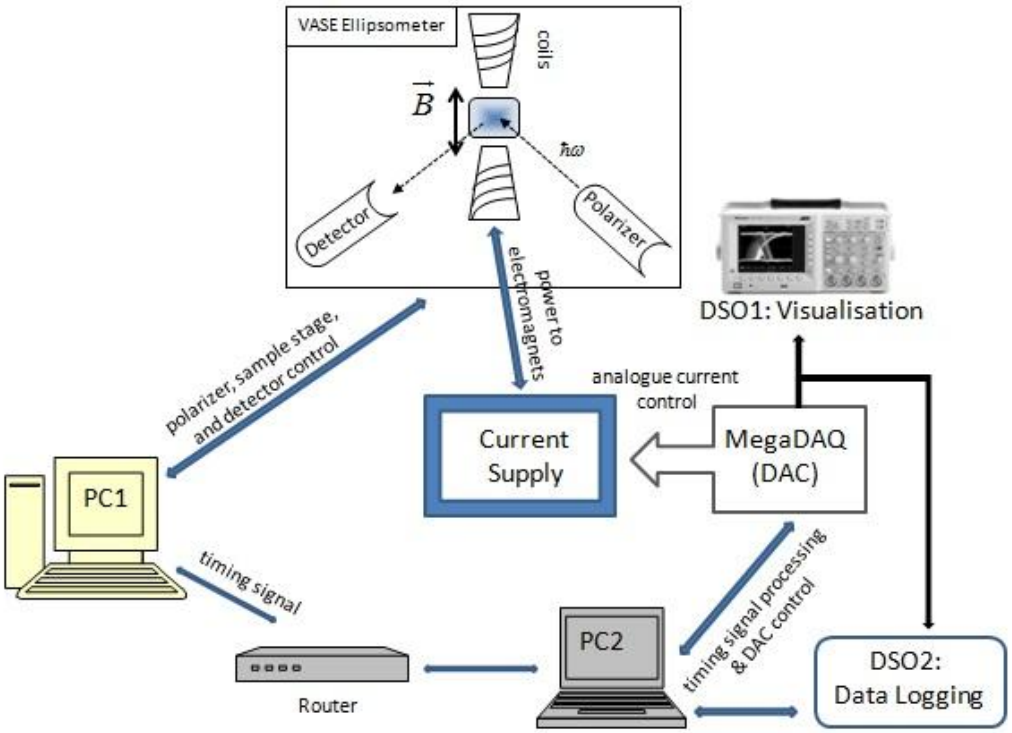

Figure III.2.6. Principal diagram of the TMOKE setup. DSO1 is Agillent DSO-X 2024A. DSO2 is a computer controlled DSO card (Picoscope 2203). The router is a generic 100mbps LAN switch.

The complete diagram of the Magnetic Field-Resolved (MFR) VASE setup is given in Fig. III.2.6. Two digital oscilloscopes (DSOs) have been attached to the output of DAC. One was used for real time visualisation of the current control voltage, while the other one, to log the magnetic field timing data for off-line data processing.

3. Vacuum techniques and deposition

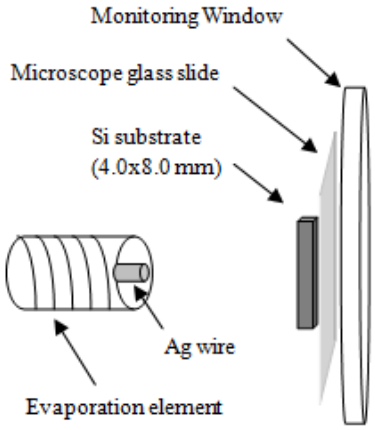

Figure III.3.1. Schematic diagram of the evaporative deposition setup.

Continuous film samples for this project had to be manufactured using the equipment available at the CAMSP. Here we describe the deposition setup that has been used to prepare samples for optical measurements. The evaporation for EELS measurements has been conducted using a similar setup and thus will not be described separately.

The deposition has been conducted in a small vacuum chamber (approx. 25 litres) made of non-magnetic stainless steel, recommissioned specifically for this task. All of the chamber's seals have been replaced with new copper and viton ones. The vacuum pumps have also been upgraded: a rotary vane backing pump[3] has been installed providing an initial pressure offset to 10^{-3} Torr, followed by 1000Hz turbomolecular pump[4]. The pressure has been monitored using a wide pressure gauge[5]. In order to accelerate the desorption rate of particles from the walls of the chamber, it has been baked three times for a total time of up to 15 hours at a temperature of 160°C using external heating elements. As a result the UHV pressure level of 10^{-9} Torr was reached.

Finally, a crucible made of alumina (see Fig. III.3.1 for a schematic), containing a piece of wire of the required material has been mounted on one of the flanges. A stainless steel substrate holder assembly has been attached to a flange with a glass window for monitoring the evaporation process (opposite to the heating element). The substrate has been cleaned with acetone and placed into the holder. A microscope glass slide has been placed between the flange and the holder to protect the window from getting opaque during deposition.

The power to the heating element was supplied using a standard laboratory current supply[6]. The deposition rate was controlled by varying the deposition time and the level of applied current.

4. Spin-Polarized Electron Energy Loss Spectroscopy (SPEELS)

Electron Energy Loss Spectroscopy (EELS) is concerned with studying the fine structure region of the spectrum determined by the energy losses mainly due to excitation of interband transitions and plasma vibrations (dipole scattering, Fig. III.4.1, region II). In EELS experiments electrons with well-defined primary energies up to a few hundred electron volts are scattered from a solid or film sample, their resulting

[3] John Moore Scientific Model 4453
[4] Pfeiffer TMH-261P Magnetic Turbomollecular Pump ($S[N_2]$ = 230 L/s)
[5] Wide range pressure gauge Vacuum Generators ATMS0435-40
[6] GW InStek GPS-1850D Lab Power Supply

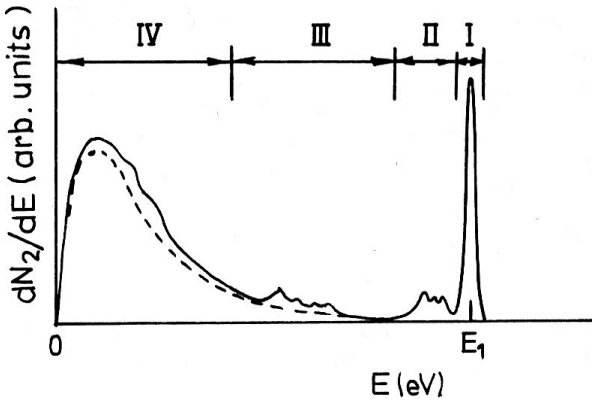

Figure III.4.1. General shape of a secondary electron distribution.
[Komolov, 1992]

energy distribution and, frequently also the angular distribution, is recorded. Due to the mean free path of electrons at such energies being only a few nanometres [Ibach, 1991], the electrons only interact with the outermost atomic layers of the material, which means that this technique is inherently suitable for characterisation of plasmon resonances in thin films.

In this work all of the electron spectroscopy analysis has been conducted using a Time-of-Flight (TOF) Spin-Polarised(SP) EELS setup. The main advantages of the TOF technique are its simplicity (hardware-wise the only principal element is the electron detector) and high efficiency due to the fact that all of the energies are measured 'in parallel'. The energy of the detected electron is determined by measuring its arrival time with respect to a nominated reference point on the time scale. The detailed description of this TOF SPEELS setup can be found in the article by Samarin [2003].

The sensitivity of the device to spin orientation allows one to study electron spin-flip processes during scattering. For example, it can be used to characterize effects of the exchange interaction. The setup has also the capability of conducting Low Energy Electron Diffraction (LEED) as well as Auger Electron (AES) Spectroscopies. These are used to determine the crystal structure of samples and their atomic composition respectively.

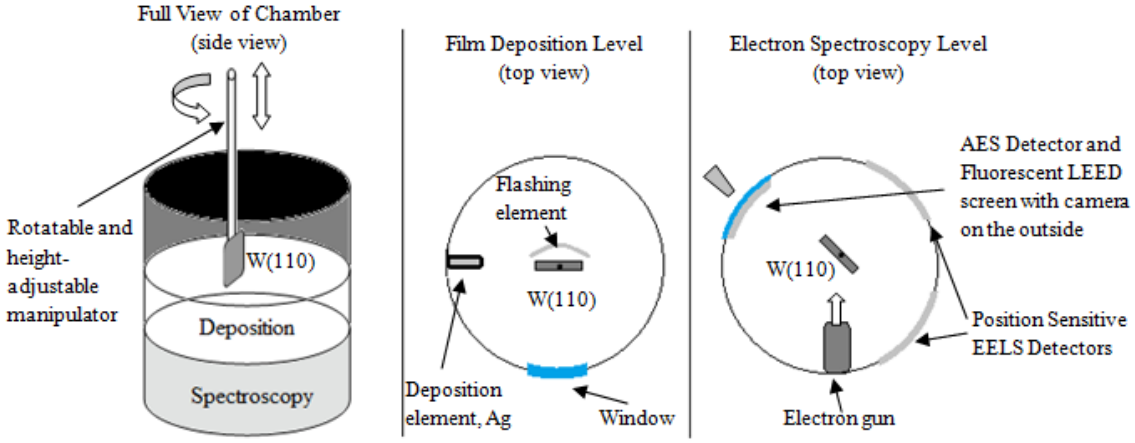

Figure III.4.2. Schematic diagram of the multi-levelled vacuum chamber used in electron spectroscopy measurements. One or both of the SPEELS detectors can be used for single or (e,2e) electron spectroscopies.

All instrumentation for this experiment was installed in a single stainless steel vacuum chamber at a pressure of 10^{-11} Torr, supported by rotary vane, turbomolecular, ion, and titanium sublimation pumps. The

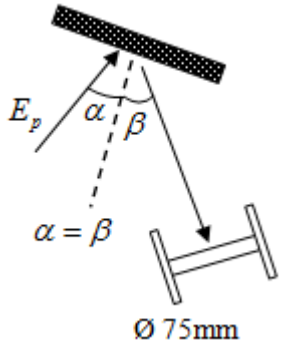

Figure III.4.3. Position sensitive EELS measurement geometry.

residual magnetic field due the Earth and surrounding external sources has been compensated by Helmholz coils placed around the chamber.

A substrate for the measurements, the W(110) crystal, was mounted on a rotatable and height-adjustable manipulator. This allowed incorporating the thermal cleaning and deposition equipment, EELS, AES and LEEDS detectors, and the corresponding electron source within the same volume (see Fig. III.4.2 for a diagram).

In order to prepare the substrate for deposition of films, the surface of W(110) has been flashed to high temperature by electron bombardment . The purity was then checked using LEEDS and AES. The comparison of the observed LEEDS diffraction pattern after flashing to that of a clean W(110) surface [Vyalykh et al., 2001] is given in Fig. VI.1.5. As can be seen from the picture, and confirmed by AES, the substrate was thoroughly cleaned. Deposition of material has been accomplished with a heating element similar to the one in Fig. III.3.1. The process of evaporation was controlled by the same technique as in section III.3.

SPEEL spectra described in this work have been acquired using a Position Sensitive detector. The measurements have been conducted in a specular geometry at an angle $\alpha = \beta = 25°$ (See Fig. III.4.3).

Part IV. Experimental results in discussion

1. Plasmons in thin films of Ag

A. Optical spectroscopy of Ag/Si thin films

Simple structures of thin films of metals on dielectric substrates have been chosen as a starting point for optical spectroscopy measurements. Plasmon studies using ellipsometry and transmission/reflection in optical regime had not been previously attempted within the group. It was therefore important to establish the feasibility of detection of plasmon excitations using this device. Although direct excitation by light does not occur in plain metal films, it is possible to use the ellipsometer to measure the dielectric function of the material to find out at which energies (or frequencies) the material supports plasmon resonances. This could then be compared to energy losses measured by Electron Energy Loss Spectroscopy. Moreover, in certain cases, such as roughness, coupling of photons to surface plasmons is possible [Jasperson et al., 1969]. Some noble metals exhibit low overall absorption losses into non-plasmonic channels, which is especially true for silver in the visible light region. Ag has therefore been chosen for the thin film. For optical measurements it has been deposited onto the Si substrate.

A number of thin film silver samples have been manufactured using the procedure described in section II.3 and characterised with the Variable Angle Spectroscopic Ellipsometer. Two types of optical experiments have conducted: measurements of ψ / Δ ellipsometric parameters and reflection spectroscopy of polarized light. The most interesting results have been obtained on a thin film that has been deposited for 5 minutes with a current of 4.2A.

The measured ellipsometric parameters for the sample are given in (Fig. IV.1.1).

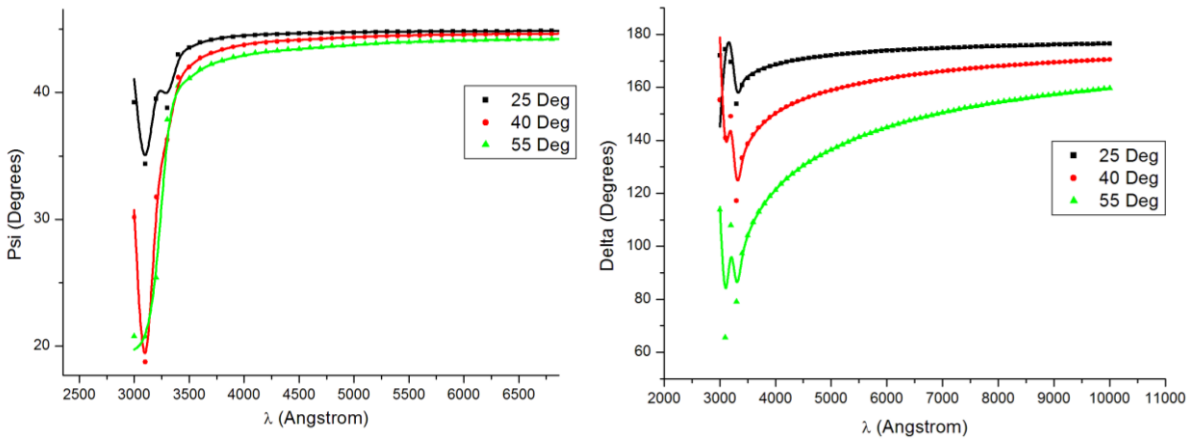

Figure IV.1.1. Ellipsometric spectrum of continuous film of Ag (sample S1, 108nm thickness) for different angles of incidence. Plot on the left: ψ vs wavelength; plot on the right: Δ vs wavelength.

The data show that the amplitude ratio of light r_p / r_s as well as the phase difference Δ are almost constant across the whole spectrum of the visible light (λ > 400 nm), indicating that there is likely no noticeable effects in this region. The near-UV region (3000Å< λ < 400Å), however, displays quite abrupt changes, suggesting possibility of resonance processes.

With the purpose of understanding the spatial scales for the observed effects, the ellipsometric parameters have been used to estimate the thickness of the Ag film.

In order to determine an optimal model for the silver film structure, first a reference Si substrate was tested with ellipsometry. The data fits have shown that there a thick layer of SiO_2 formed at the interface of the substrate with air:

Substance	Thickness
SiO_2	30.496 ± 0.167 nm
Si Substrate	0.3 mm

The large thickness of the silicon dioxide layer is not surprising, since the substrate was quite old and had not been treated in any special way to remove the layer. After determining the optimal layer model the following thickness estimates have been generated for the sample:

Substance	Thickness
Ag	108.389 ± 5.3 nm
SiO_2	19.050 ± 13.3 nm
Si Substrate	0.3 mm

The model was found to replicate the results very accurately, with the mean square root error being only 1.253 when the resulting refractive index was fitted (see Appendix A).

Analysis of previous works has shown that quite often phenomena attributed to plasmons are found in the reflectivity spectrum. The reflectance intensities for both *s*- and *p*-polarized incident beams have been measured in two consecutive experiments. The data has been compensated for background noise, transmission properties of air and non-linearity of the detector by conducting a preliminary baseline transmission measurement. The statistical error in *R* was estimated to be ≈±0.025.

The reflectivity amplitude of the order of ~0.9 was observed for the long wavelength region (λ=500-1000 nm), which is a common feature in metals due to electrons screening the electric field of light at frequencies $\omega < \omega_p$. In the blue and near-UV region, however, multiple minima of reflection have been found suggesting strong resonant absorption. Some of the features were noticably missing for an *s*-polarized incident beam. This part of the spectrum is shown in detail in Fig. IV.1.2.

The most striking aspect of the R_p spectrum is the almost complete absorption of light at 3120Å (peak *A*) with a region of low level reflectivity for smaller λ. Smaller absorption peaks *B* and *C* are also seen. In order to establish whether any of these features could be attributed to plasmons, it is important to consider the requirements for such a resonance to exist. These requirements were given in chapter II and require knowledge of the dielectric constant of the material. The pseudo-dielectric function of the sample measured for this purpose with ellipsometry can be found in Appendix A.

The dielectric function can be converted into two 'pseudo' Loss Functions by using a simple algebraic transformation. These functions contain maxima at the points which satisfy plasmon resonance conditions and are an effective way to visualise plasmon-related losses. The bulk loss function is given by [Steel, 1972]:

$$-\mathrm{Im}\left(\frac{1}{\varepsilon}\right)=\frac{\varepsilon_2}{\varepsilon_1^{\,2}+\varepsilon_2^{\,2}}=L_b, \qquad \text{(IV.1.1)}$$

whereas the surface losses can be determined from [Ibach, Luth, 2010]:

$$L_s=-\omega\,\mathrm{Im}\left[\frac{1}{(\varepsilon_1+i\varepsilon_2)+1}\right]. \qquad \text{(IV.1.2)}$$

As seen from the graph (Fig. IV.1.3), the theoretical surface plasmon resonance condition is satisfied, with $\tilde{\varepsilon}_1=-1$, at $\lambda_{sp}=3404$ Å (Peak *C*). In the reflectivity spectrum (Fig. IV.1.2), the resonance wavelength corresponds to the middle of the broad dip *C*.

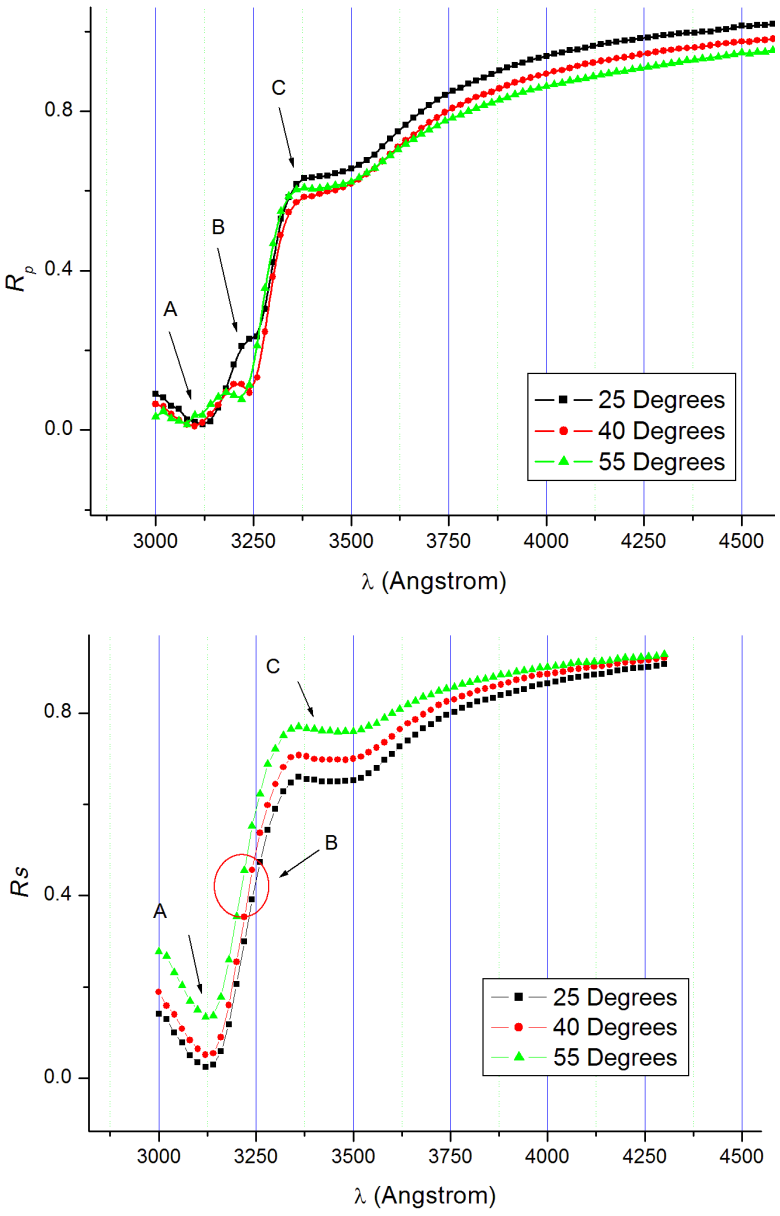

Figure IV.1.2. Reflectance spectrum of continuous film of Ag (sample S1, 108nm thickness) for different angles of incidence. Top figure: Incident beam *p*-polarized; bottom figure: Incident beam *s*-polarized.. Data were measured with a step size of 20nm.

Even though the dielectric loss function shows that surface plasmons are allowed at the position of Peak C, this does not immediately imply that the SP resonance is excited. Photons incident onto a flat thin film of metal typically

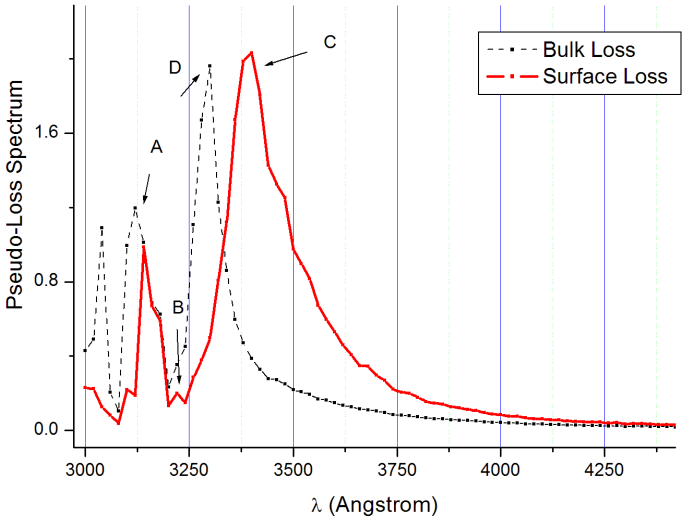

Figure III.1.3. Pseudo-dielectric loss function of continuous film of Ag (sample S1, 108nm thickness). Data were measured with a step size of 20nm.

do not possess the right momentum to cross the plasmon dispersion line (see Fig. II.1.3). Moreover, the effect is seen in both polarizations. This contradicts the general theory stating that surface plasmons can only be excited by *p*-polarized light.

On the other hand, very similar effects have been observed by Jasperson et al. [1969] in thick silver foils. For comparison, their reflectivity spectrum is given in Fig. IV.1.4. In that work, the resonance absorption had been explained by the naturally occurring surface irregularities of dimensions comparable to the surface-plasmon wavelength. Surface roughness causes scattering and diffraction of incident light and modifies its vector by Δk_x. Due to the presence of these new spectral components the incident light line $k = \omega / c$ crosses the surface plasmon dispersion curve:

$$k_x = k \sin(\omega / c) \pm \Delta k_x = k_{sp} . \quad \text{(IV.1.3)}$$

Raether (1988) also states that numerous experimental results have shown that nonradiative surface plasmons tend to interact via surface roughness. He explicitly points out that for rough surfaces multiple scattering can result in rotation of the wavevector in plane, which would relax the requirement for the polarization of incident light.

Photon-plasmon coupling in our silver film due to roughness appears to be the most likely cause of the resonance minimum at 3400Å. Although silicon is known for its flatness, in our case it is covered with a thick layer of SiO_2. Electron spectroscopy measurements [Nakayama et al., 1991], have established that oxide polymers forming on the surface of Si tend to appear in clusters. Combined with the fact that evaporative deposition may lead to formation of nanoscale droplets on the surface the film, the sample surface might indeed be uneven. In order to prove this argument however, a detailed surface analysis of the sample will be required. Although surface roughness can be integrated into ellipsometric models to deduce thickness, it is not easy to use the technique in reverse. In most cases roughness thickness

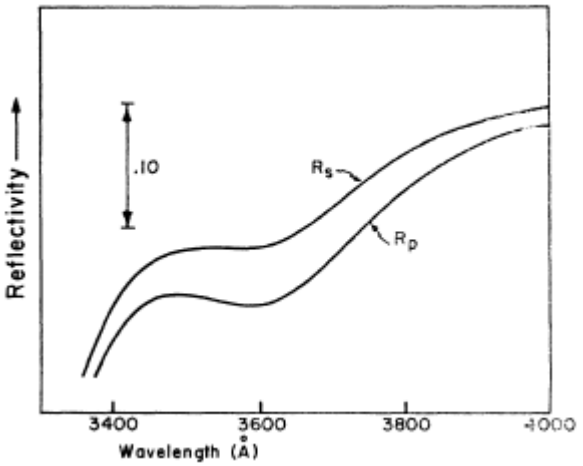

Figure IV.1.4. Reflectance spectrum of Ag film for an incident angle of 45 Degrees. [Jasperson et al., 1969].

will correlate very strongly to the thickness of the film, and usually the unevenness is either not included in the analysis or has to be fixed manually at some reasonable value (VASE Manual).

Going back to the pseudo loss spectrum, a Peak *D* is found in the bulk loss spectrum at 3300Å, which corresponds to the formal condition $\varepsilon = 0$ for a bulk plasmon resonance. However, as explained by Taneja et al. [2002], an onset of interband transitions occurs in silver at $\hbar\omega = 3.9$ eV (3180Å). These transitions result in an additional contribution to the free-electron dielectric function due to bound electrons. In thin films this gives rise not to a bulk but to a *hybrid* plasma resonance. A resonance of this type would explain the presence of Peak *A* in both bulk and surface loss spectra and the high absorption around the 3100-3200 Å point.

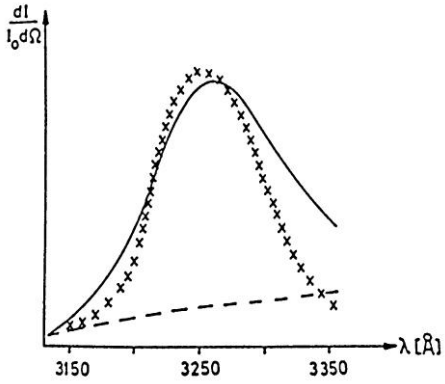

Figure IV.1.5. Light intestity of scattered SPs around the plasma frequency of silver (50nm thick), 30° specular reflection. Continuous curve: calculated volume contribution; dashed curve: calculated surface contribution; (xxx): observations. [Raether, 1988]

The nature of the maximum *B* in reflection is not apparent from the pseudo loss spectrum. This peak has to be somehow linked to the polarization of the incident light, since the feature is missing in R_s. Furthermore, the position of the resonance is shifted towards higher energies and with an increase in the incidence angle. Reflectivity is also increased accordingly. In the literature, this dependence was mainly related to surface plasmon measurements in transmission, where photon-surface plasmon coupling due to roughness resulted in resonant emission of light on the other side of the film. This effect is only possible for *p*-polarized light due to momentum conservation and will be strongly dependent on the angle. However, as Raether [1988] points out, an analogous effect is possible in reflection. It is caused not by surface roughness, but by volume (or interior) roughness. *P*-polarized light is scattered on the internal irregularities of the material and the continuum of roughness vectors redistributes wavevectors of radiation to cross the plasmon dispersion curve. The detected feature in reflection (Fig. IV.1.2) could in fact be a minimum corresponding to the excitation of plasmons inside the interfaces of the material. The superimposed maximum in intensity would then point to the radiative decay of plasmons and scattering of the emission over a large angular region outside the surface, see Fig. IV.1.5. This explanation would tie in very well with the hypothesis of the SiO_2 layer roughness due to clustered polymerisation.

B. Ag/W(110): Electron Spectroscopy Study

In order to verify some of the conclusions which follow from the optical spectroscopy measurements, Spin-Polarized Electron Energy Loss Spectroscopy (SPEELS) was also conducted on thin films of silver. EELS has been reported as one of the most efficient techniques to observe and study plasmon excitations in

noble metals [Pulisciano, 2008]. Consistency between optical and electron spectroscopy measurements was thus likely to provide us with a strong indication on whether the observed effects could be attributed to plasmon resonances.

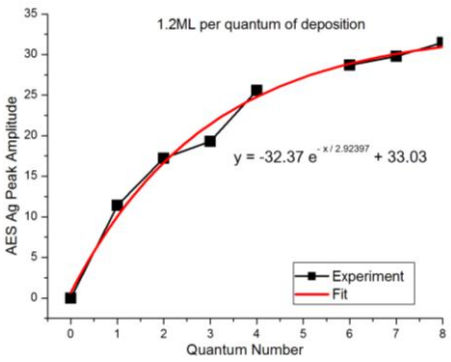

Figure IV.1.5. Deposition thickness calibration curve measured with AES. $\tau = 2.92397$.

The current research at CAMSP is focused on investigating electron properties of films deposited on top of a W(110) crystal substrate. By the time of the beginning of the present Honours project the experimental setup, described in section III.4, had been configured for electron spectroscopy measurements of films on W(110) single-crystal substrates and any modifications to it would have interfered with that ongoing research. Ag/W(110) was therefore the closest structure to Ag/Si that could be analysed in this setting.

A number of samples of Ag/W(110) with Ag films of different thicknesses have been fabricated using the vacuum evaporation technique with deposition times ranging from 3 to 9 minutes and current of 4.21A.

Auger Electron spectra (AES) have been recorded for each of these samples. Comparison of the results to reference values has shown Auger electron emission peaks characteristic of silver atoms. This has confirmed that layers of Ag have been successfully deposited onto the W(110) substrate. Furthermore, it is known that the amplitude of an AES peak that corresponds to silver depends on the evaporation time via an exponential relationship: $A \propto -e^{-x/\tau} + const$, where x is the quantum of time (in our case – 3 minutes). The τ-parameter is linked to the mean free path of electrons in silver. The above specified exponential dependence was fitted to the plots of AES amplitudes vs quantum number x (Fig. IV.1.5). The parameter was estimated to be around 2.9. Comparison to a commonly accepted value of τ =8.2 Å, has indicated that in a single quantum of deposition a layer of 8.2/2.9 = 3.5Å of silver is deposited. This is equivalent to1.2 monolayers (1 monolayer ~ 2.36Å).

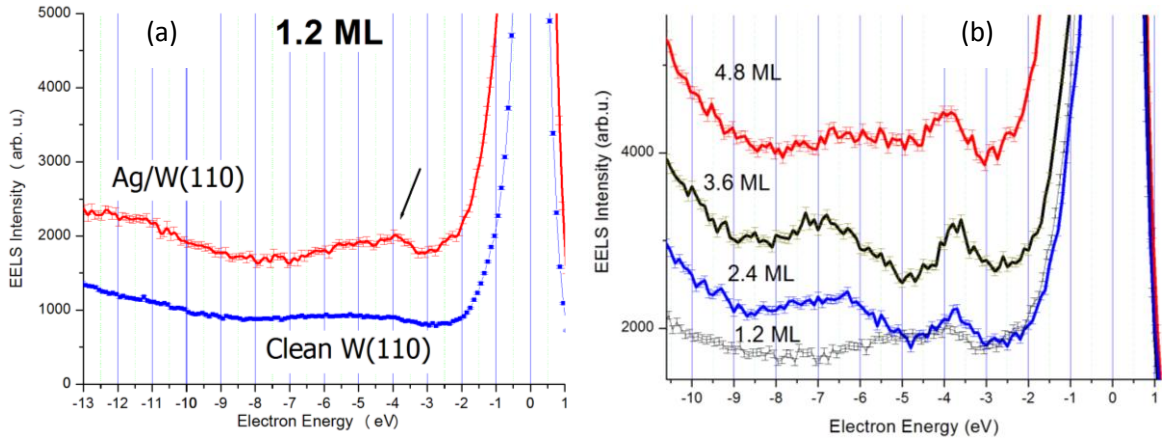

Figure IV.1.6. (a) Comparison of EELS spectrum of Ag/W(110) with that of a pure substrate. (b) Comparison of EELS spectra of Ag/W(110) of different thicknesses. Notice the peak at 3-4 eV.

Electron energy loss spectra of Ag thin film samples of thicknesses ranging from 1.2 to 4.8 monolayers (MLs) have been recorded. The measurements have been conducted with a primary electron energy of 17 eV. A SPEELS spectrum of a clean W(110) has also been obtained for reference.

Starting right from the thinnest sample (1.2 ML), an energy loss peak has been observed at around 4 eV. The comparison with W(110) spectrum has shown that the feature is inherently related to the silver film (Fig. IV.1.6 (a)). The monotonous increase after about 9 eV appears to follow the trend of W(110).

Comparison of films of different thicknesses reveals a second peak around 7-8 eV (Fig. IV.1.6 (b)). It slightly grows with monolayer count, but then almost completely disappears when the film reaches a thickness of 4-5 monolayers. This effect could be due to the different crystal structure of silver. Typically, as the silver film with a bcc lattice structure (111) grows on the fcc surface of W(110), in very thin films (heteroepitaxial growth) it can form islands that cause additional electron scattering. Another explanation could be that this peak is caused by multiple overlapping interband transition states. These states seem to correspond to energy losses that we have seen during optical studies: they appeared as multiple peaks in both the pseudo loss spectra of bulk and surface contributions (Fig. III.1.3, $\lambda < 3150$Å). As calculated by Taneja et al. [2002], 3.9 eV marks the continuum of transitions from the quasicontinuous electronic energy levels of the *d* energy band to the *s* band and beyond.

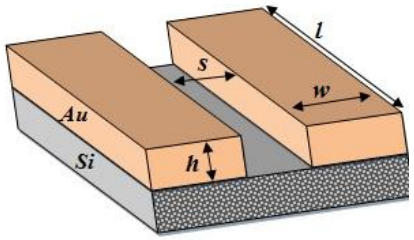

Fugure IV.2.1. Schematic diagram of the Au nanostripe array sample.

Referring back to the first peak, it can be seen that as the film grows, the maximum becomes sharper. At a thickness of 4.8 ML, though, it starts to get obscured by the continuum. The centre of the peak corresponds to the energy of 3.75 eV. When converted to frequency via $E = \hbar\omega$, this value equals to the wavelength of 3310Å. Similar maxima have been obtained by EELS studies of free-standing silver crystals of different lattice structures [Rocca et al., 1990]. Interestingly, the energies for the maxima obtained in a number of different studies [e.g. Rocca et al., 1990; Pulisciano et al., 2008] ranged from 3.65 to 3.8 eV. These values are in line with our estimates of 3.65 eV to 3.85 eV (3150Å-3400Å, Fig. III.1.3) for a plasmon resonance. In this context, we can hence conclude that in thin films of silver there exists an overlapping state of interconnected hybrid and surface plasmon modes, which is located around 3.65-3.8 eV (3200-3400Å).

2. Surface Plasmon-Polaritons in Nanostripes

We have shown on the example of a thin film of silver (see section IV.1) that surface roughness has the potential to couple photons of incident radiation to surface plasmon modes. Mathematically, roughness effects can be understood by considering a superposition of an infinite number of gratings of different geometric parameters. While diffraction from some of these ‘gratings’ adjusts the radiation wavevector to

match plasmonic resonances, most of the light simply scatters in arbitrary directions resulting in a loss of energy. As a consequence, implementing this coupling channel in plasmonic circuitry would be rather difficult. It would therefore be of great interest to develop thin film systems with highly ordered periodic structures that are optimized to induce plasmonic modes without dissipating much energy.

As was mentioned in the overview (Section II), the current research on periodic structures has so far concentrated on plasmons and plasmon-mediated enhancements of electromagnetic and optical properties of nanoscale gratings. A grating typically consists of a single-layer or multilayered film of metal that is grooved, but not perforated. While the experiments have shown that this geometry is very effective at generating surface plasmons, the entire metal film remains a single conductive crystal. On the other hand, in electronic-plasmonic circuitry it might be beneficial to break up the grating into separate stripes, with each conductor carrying separate currents. Only a few very recent studies have characterized plasmonic effects in such structures, with the conductive layer consisting of a non-magnetic noble metal [Belotelov et al., 2009; Belotelov et al, 2010].

In this project we analyse and compare nanostructures in the form of one-dimensional arrays of parallel nanostripes made from the following metals: non-magnetic gold and ferromagnetic Permalloy. They have been manufactured at the National University of Singapore by a process of Deep UV lithography followed by lift-off [Adeyeye and Singh, 2008]. This recently developed high-precision technology allows one fabricating unique macro-sized dense arrays (approximately 0.5x0.5 cm^2) of nanoelements with a very narrow distribution of parameters. A number of such samples have been prepared, with structure periods of ~370 to 500 nm and stripe thickness of 100 nm. Surface plasmon excitations in these periodically nanostructured films have been observed using ellipsometry and reflectivity spectroscopies. The macro-scale sizes of the samples have allowed one for the first time to use a standard wide-beam ellipsometer to characterise such structures.

A. Au Nanostripes on Si Substrate

In this experiment we characterized a sample with nanostripes made of gold and deposited onto a silicon substrate. The stripes are continuous over the whole length of sample. The geometry of the system is shown in Fig. IV.2.1 and summarized in the following table:

Physical size (l)	Height of Au layer (h)	Width of stripe (w)	Stripe separation (s)
0.5x0.5 cm	100 nm	264 nm	113 nm
Maximum deviation: ±9 nm			
Period: $d = w + s = 377$ nm			

Reflectivity measurements have been conducted on the structure for the following configurations:

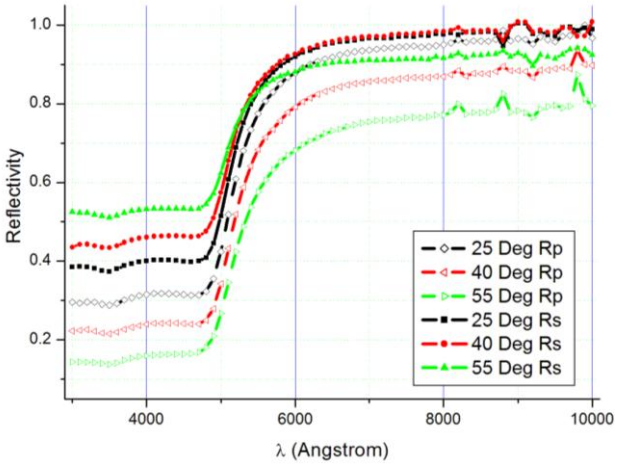

Fugure IV.2.2. Reflectivity spectra for a 100nm-thick reference Au film for *s*- and *p*-polarised incident beams.

- nanostripes in the plane of light beam incidence;
- nanostripes perpendicular to the plane of light beam incidence.

The goal of this measurement is to provide us with reference data for the characterisation of the effects in Permalloy stripes.

A continuous 100 nm thick Au film reference sample manufactured in the same process was also tested for comparison (Fig. IV.2.2). The data have been obtained for both *s*- and *p*-polarized incident beams. Detailed diagrams of the measurement geometries can be found in Appendix D. Statistical error was no more than ±0.025.

Figures IV.2.3 (a) and (b) illustrate *p*- and *s*-polarized reflectivity spectra measured at incident angles ranging from 25 to 65 degrees with nanostripes aligned perpendicular to the plane of incidence.

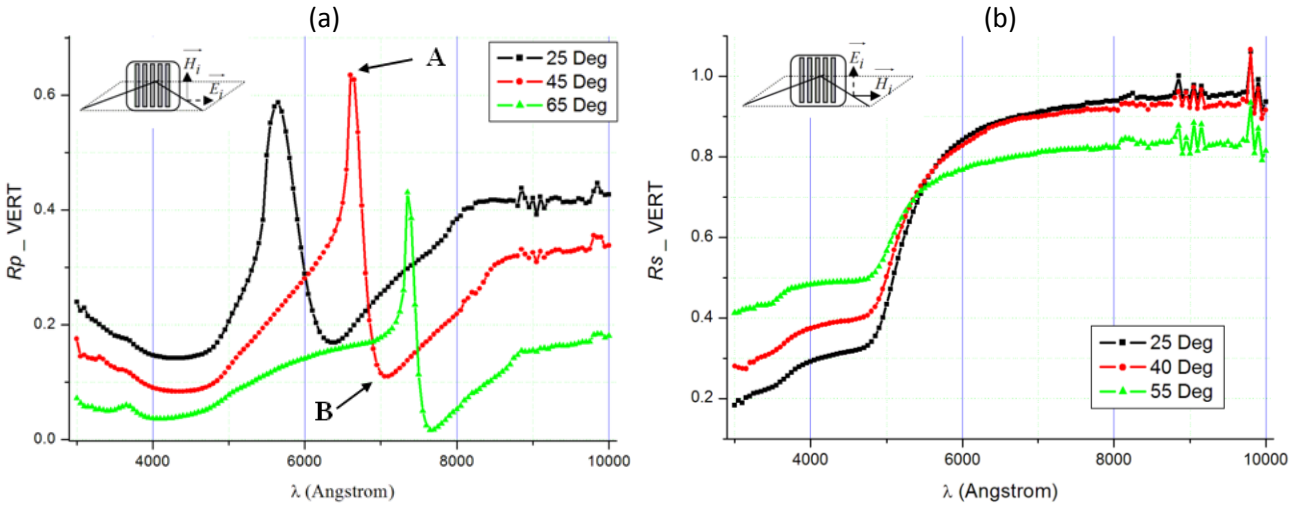

Figure IV.2.3. Reflectivity spectra of a gold nanostripe array of *d*=377nm with stripes perpendicular to plane of incidence. (a) Incident beam is *p*-polarized. (b) Incident beam is *s*-polarized.

As can be seen in Fig. IV.2.3, whereas the *s*-polarized reflectivity is very similar compared to the data obtained on the reference film, the reflection in R_p is dominated by a sharp resonance maximum (Peak A). This maximum shifts by a significant value (~400-500 nm) and changes its shape with an increase in incidence angle. The asymmetric profile of the maximum, especially for larger angles, appears to indicate that the peak is a Fano-type resonance. This type of resonance is usually associated with two different processes which interfere with each other. Moreover, to the left of the peak, in the region (3000-5000 Å), a much higher absorption level is observed than in the R_s spectrum. The absorption is almost complete at $65°$ in the R_p spectrum.

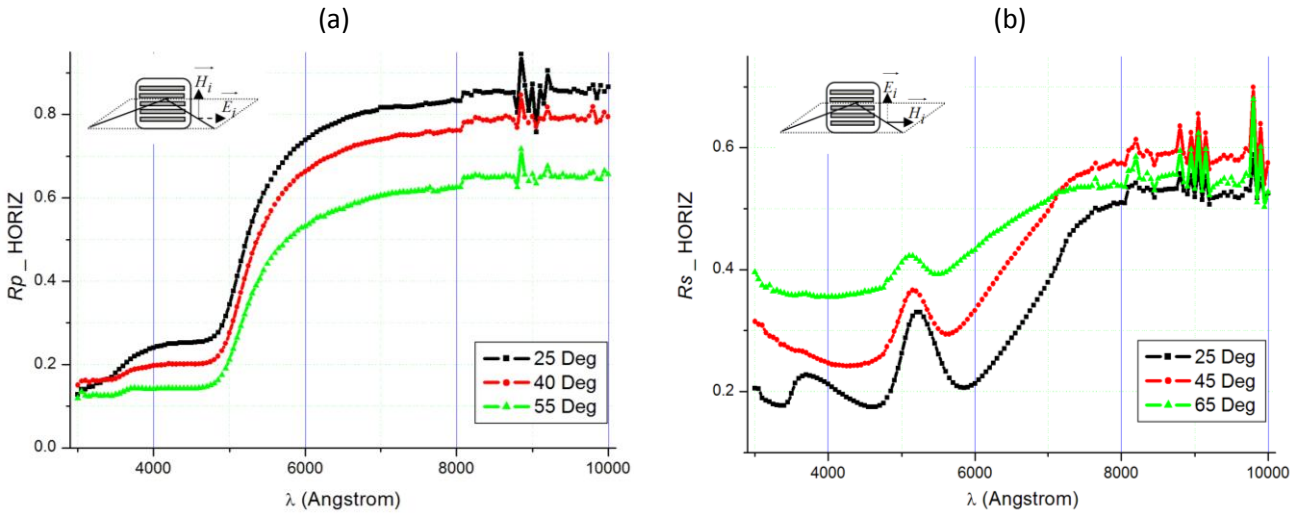

Figure IV.2.4. Reflectivity spectra of a gold nanostripe array of *d*=377nm with stripes parallel to plane of incidence. (a) Incident beam *p*-polarized. (b) Incident beam *s*-polarized.

Reflectivity of the sample measured with stripes oriented parallel to the plane of incidence of light has also shown polarisation-dependent behaviour. A resonance maximum is observed this time in *s*-polarisation (Fig. IV.2.4(b)), albeit at different wavelengths than in Fig. IV.2.3(a) . A change in R_p (Fig. IV.2.4(a)) is also evident, with the reflectivity now closely following the curve for the reference film sample.

The swap in resonance features for the R_p and R_s curves that occurs after rotating the sample by 90 degrees indicates that the phenomena should be linked to the polarisation of electromagnetic field of the incident light and to the geometry of the sample. Resonance features appear to be induced only when the electric field of the incident light is perpendicular to the metal stripes.

The nature of the peaks should obviously be related to diffraction effects on a periodical lattice. It is known that regular periodic structures can exhibit abrupt changes in reflection, which are referred to as Wood Anomalies [Wood, 1902]. For regular arrays of nanoparticles on a transparent substrate these anomalies have been interpreted by Rayleigh [1907] as disappearance of a diffracted beam when it crosses the boundary between the ambient medium and the substrate. In gratings, if the light is *p*-polarized, the resonance maxima should simply correspond to the diffraction in the first order with the (first order) diffracted beam along the surface of the sample. This condition is given by the equation:

$$\lambda_{Wood} = d(1+\sin(\theta)), \quad \text{(IV.2.1)}$$

where θ is the angle of incidence.

It turns out, that as a result of this diffraction, the electric field

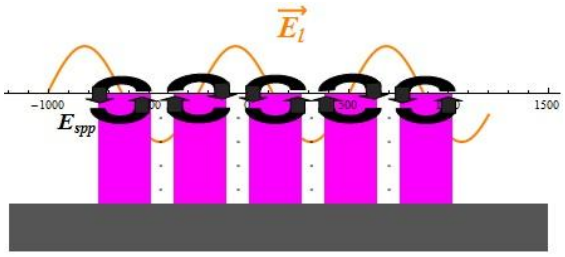

Figure IV.2.5 An intuitive illustration of excitation of coupled SPP modes in gratings. The wave is the electric field of light propagating along the surface.

of *p*-polarized light has the ability to excite surface plasmon-polaritons in the grating [Grunin et al., 2010]. These SPP modes will depend on the material and will manifest themselves as absorption peaks in the reflectivity spectra at resonance wavelengths given by:

$$\lambda_{SPP} = d\left(\sqrt{\varepsilon_{metal}/(\varepsilon_{metal}+1)} + \sin(\theta)\right). \quad \text{(IV.2.2)}$$

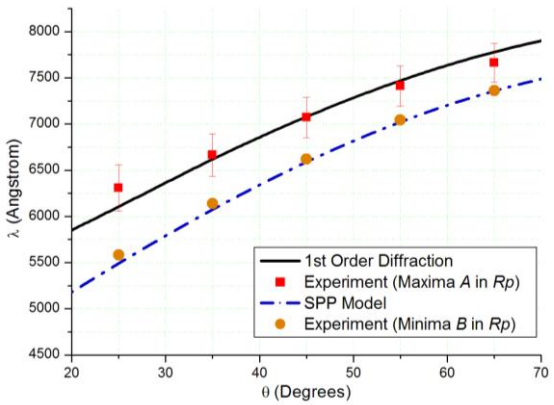

Figure IV.2.6 Fit of Wood's Anomaly and SPP conditions to *Rp* reflectivity data of Au nanostripes. *d*=384nm.

Due to momentum and energy conservation laws, the surface plasmon will be located near the right 'wing' of the Wood's Anomaly in the reflection spectrum [Gippius et al., 2005]. The electric fields associated with the surface plasmon excitations in each of the stripes of the grating will be significantly enhanced due to coupling to neighbouring stripes by the incident light [Kravets et al., 2008].

The fitting of resonance conditions (IV.2.1) and (IV.2.2) has been done by taking peaks *A* as Wood's anomalies and minima *B* (Fig. IV.2.3) as the excited SPPs. Given the error in *d* of ±9nm, the best fits have been achieved with *d*=384nm. The dielectric function of gold has been measured separately on the reference film. The fits are given in Fig. IV.2.6. As can be seen, the resonance condition for the Wood's anomaly fits the spectrum almost perfectly. There is a small deviation in the location of resonances of plasmons however. Most likely, the condition (IV.2.2) is not completely suitable to perforated samples, such as the arrays of nanostripes. As Mayer [2007] notes, in systems with grooves more than 20nm high scattering paths usually offset the parameters. Considering the phenomenon of extraordinary transmission observed in perforated slits [Belotelov et al., 2009], the substrate can also contribute to the effect. Another possibility is the excitation of a localized plasmon mode in the immediate vicinity of the SPP (see Fig. IV.2.7). The existence of such modes has been theoretically shown by Belotelov et al. [2009] for structures with geometry very similar to ours.

In any case, the reflectivity data have given strong indication of existence of plasmon resonances in the nanostripe structures. The Fano-resonance peaks due to the Wood's anomaly and the suspected SPP are very sharp and their position and form can be controlled by altering the angle of incidence of the beam.

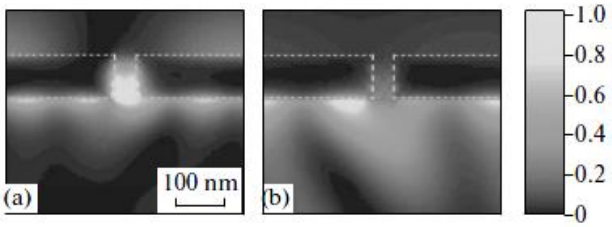

Figure IV.2.7. Magnetic field of a combined SPP/Localized Plasmon (a) vs SPP-only mode (b). [Belotelov, 2009]

B. 1D Permalloy Nanostripe Array

As a next step, reflectivity spectra of nanostripe samples made from a ferromagnetic material –Permalloy-have been measured. Permalloy is an alloy which consists of 80% of nickel and 20% of iron (Fig. IV.2.8).

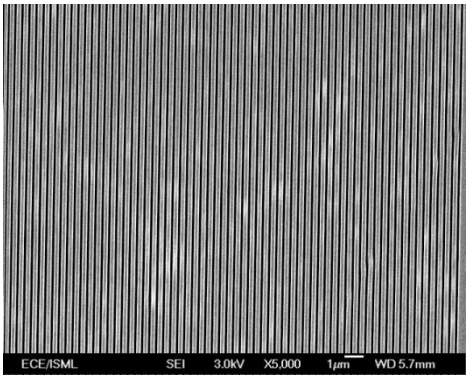

Fugure IV.2.8. Scanning electron micrograph of 1D dense nanowire array of Permalloy.

The reflectivity spectra of R_p and R_s measured with stripes perpendicular to the plane of incidence are given in Fig. IV.2.9. The sample used in this case had the same dimensions as the Au one.

As one can see from the graph, the different polarisations of light once again produce completely different spectral profiles. In R_s the spectra are relatively plain with a monotonous increase in absorption towards the UV region, similar to the Au sample. The spectrum for the *p*-polarised also has the peaks closely matching the ones for the gold nanostripes. Measurements of spectra with stripes parallel to the plane of incidence also produced results analogous to the ones of Au.

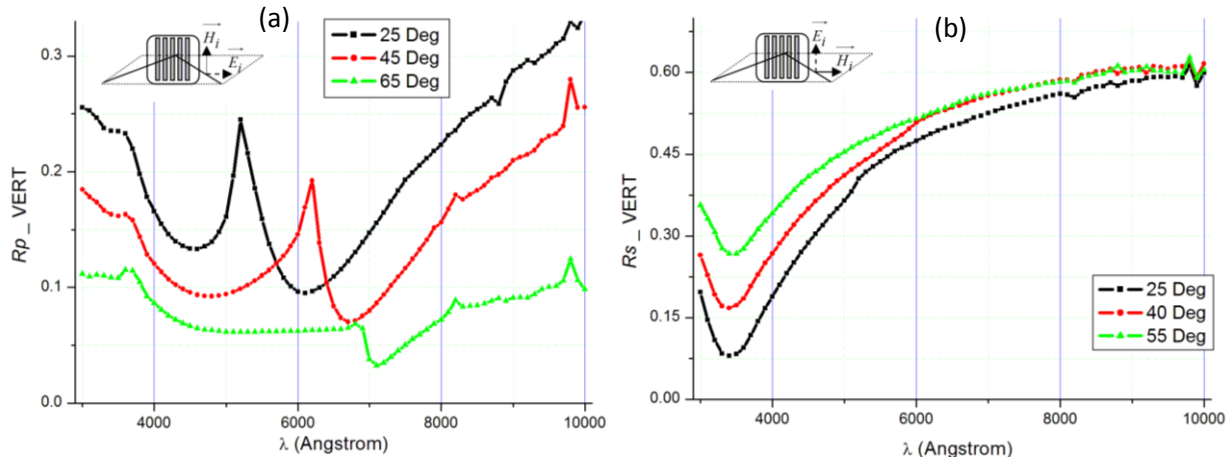

Figure IV.2.9. Reflectivity spectra of a Permalloy nanostripe array with *d*=377nm. Stripes are perpendicular to plane of incidence. (a) Incident beam is *p*-polarized. (b) Incident beam is *s*-polarized.

Fitting of models (IV.2.1) and (IV.2.2) have been performed for Permalloy samples as well. As before, the Wood's Anomaly condition has shown an excellent agreement with experimental results. The SPP condition showed similar slight deviation from the perfect fit as in the case of Au.

In order to understand the effect of material properties, we can select a reflectivity spectrum for one incidence angle for Permalloy and compare it to the data obtained on the Au structure. This plot is given in Fig. IV.2.10. As can be seen, first of all, the Permalloy sample shows much higher overall absorption.

The full-width half-maxima of the peaks in reflectivity of Permalloy are about 4 times larger than that of Au. The amplitudes of the maxima have dropped by about a factor of 3. This is not surprising: as discussed in section IV.A, noble metals exhibit much lower absorption than transition metals. A more interesting effect occurs when the minimum *B* is considered.

The resonance is broader in $Ni_{80}Fe_{20}$, and its extremum is shifted. This absorption-peak broadening is consistent with excitation of plasmons in the system: Permalloy has a much higher imaginary part of ε than gold (see Appendix D for comparison), which should result in significant damping of the resonance, i.e. spread in frequency over a larger region. The latter should be seen as a broader absorption peak of smaller amplitude, similar to what one sees in the figure. The shift in the resonance frequency is also explained by the change in the dielectric function of the material. However, as eqn. IV.2.2 shows, its position is still dependent on the period of the structure. The explicit dependence on the period has also been tested (see section IV.3.B).

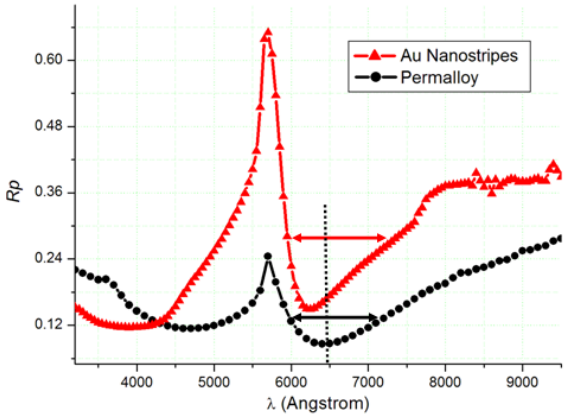

Figure IV.2.10. Reflectivity spectra of Permalloy vs Au nanostripes. The dashed line shows the plasmon absorption peak for NiFe. (The data have been manually shifted to align at Wood's maxima to compensate for deviation in period *d*)

3. Plasmon-enhanced Transverse Magneto-Optical Kerr Effect in nanostructures

A. MFR VASE Setup Verification: Non-magnetic Noble Metals and Hysteresis Loop for Continuous $Ni_{80}Fe_{20}$ Film

The assembled electromagnet attachment to the VASE has been calibrated with a magnetometer: the dependence of the magnetic field at the position of the sample on current has been recorded. Since the magnetometer could not be used during ellipsometry measurements, as it would obscure the light beam, these calibration data were used to obtain values of the magnetic field during TMOKE experiments. It has turned out that the field strength in the space between the magnet poles made from soft iron can easily reach 1000 Oe and this value is within the safe operating limit of the solenoid (~4.2 A). This is well above the value required to magnetically saturate the Permalloy samples. For all typical measurements, it was enough to apply fields below 300 Oe (~1.5 A). The downside of using the soft iron cores was that they exhibited a small hysteresis (~10 Oe) which had to be compensated for when processing the raw output data.

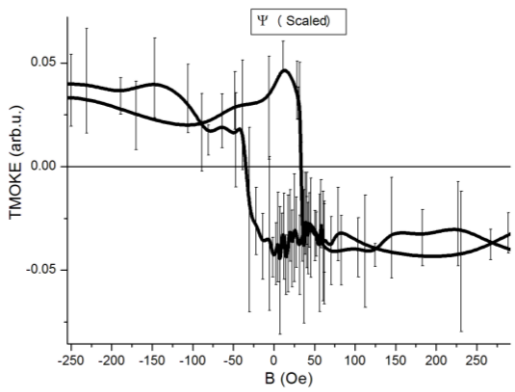

Fugure IV.3.1. Hysteresis loop of a 100nm reference Permalloy/Si film measured by MFR Ellipsometry at 35° incidence angle.

In order to test the functionality of the magnetic field-resolved (MFR) system and to find out whether the sensitivity of VASE was high enough to detect the transverse MOKE signal, a hysteresis loop of a continuous film of Permalloy has been taken with the setup. For this measurement, a wavelength of 4500Å has been chosen and values of ψ / Δ have been recorded as a function of applied magnetic field. A characteristic hysteresis loop has been successfully recorded for the material (see Fig. IV.3.1). It has been found that the field strength required to fully saturate the film was about 35 Oe, which agreed well with ferromagnetic resonance experiments (the saturation field of 100-200Oe discussed earlier was required for perforated samples).

The success in recording a hysteresis loop implied that the transverse MOKE could be reliably measured over the complete accessible optical spectrum. The experiment has been run over the range of $\lambda = 4000 - 8000$ Å, for which the ellipsometer has the lowest measurement error. Each point has been measured 8 times – four times in one direction of $\vec{B}$ and four in the opposite. This allowed us to accumulate a reasonable statistical certainty in the data. To quantify the TMOKE effect we used the following:

$$\theta_{\psi} = R_{\vec{B}\uparrow} - R_{\vec{B}\downarrow}, \text{ where } R = R_p = \tan(\psi)^2 R_s ; \quad \text{(IV.3.1)}$$

$$\theta_{\Delta} = \Delta_{\vec{B}\uparrow} - \Delta_{\vec{B}\downarrow}.$$

The TMOKE function for the Permalloy film is shown in Fig. IV.3.3.

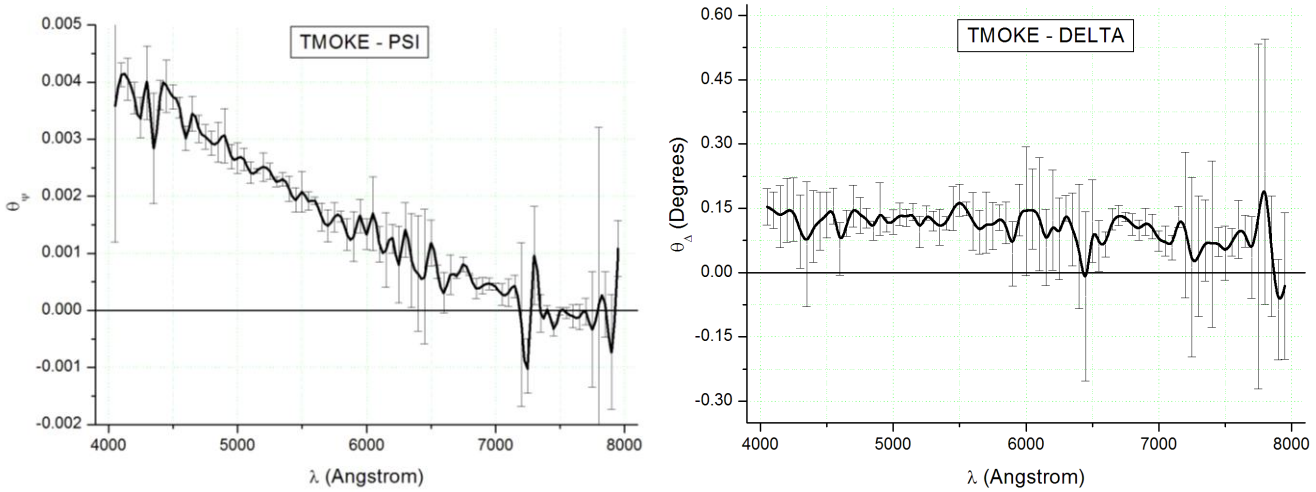

Figure IV.3.2. Transverse MOKE effect measured on a 100nm continuous film Permalloy sample. Incidence angle is 35 Degrees. Magnetic field was set to ±250 Oe to fully saturate the samples.

As can be seen from the graph, ψ demonstrates an approximately linear dependence of θ_{ψ} (change in reflectivity due to MOKE) on light wavelength. It is largest for low values of λ. The variation in the phase of the reflected *p*-polarized beam is very small and approximately constant across the full spectrum of the visible light.

Finally, a test TMOKE measurement has been taken on a continuous gold film in the range $\lambda = 4000$-8000nm. Since Au is a non-magnetic metal, no Kerr effect was expected over the whole spectrum. A change in the output with application of $\vec{B}$ would indicate that the observed effects are coming from sources other than TMOKE. The experiments on Au with $\vec{B}$ ranging from ±100 to ±1000 Oe have consistently shown that there is no Kerr signal for noble metals, confirming that the effect observed in ferromagnetic samples was due to the transverse MOKE.

B. Ferromagnetic periodic nanostructures

Recent reports indicated that enhancement of Transverse Magneto-Optical Kerr Effect (see Literature Overview Section) is possible in one-dimensional nanogratings made of magnetic metals. In this view, transverse MOKE spectrum of the 1D nanostripe arrays was measured using the magnetic-field-resolved VASE setup.

The magneto-optical Kerr effect spectrum has been recorded in the spectral range of 4000-8000Å. All the measurements have been conducted with a beam incidence angle of 35°. This was found to be the optimal setting to minimize diffraction from the edges of the small sample and to ensure that the light beam is not obscured by the electromagnet. The magnetic field was set to ±250 Oe, as in the experiments on continuous films. The TMOKE data were averaged over a sample size of 8 modulations in $\vec{B}$, as before.

The TMOKE spectrum measured for a Permalloy nanostripe sample of period 377 nm is given in Fig. IV.3.1.

When compared to the Permalloy reference sample (Fig. IV.3.3), it can be seen that the TMOKE function has changed completely. Instead of the almost linear decrease in θ_{ψ}, this time the Transverse MOKE is almost constant at small wavelengths (400-550nm). At about 6150-6250Å there is an enhancement peak, with the gain in intensity of about a factor of 2.5, when compared to the reference-film TMOKE values at the same wavelength. A phase change in Δ can also be noticed that occurs at about 5700Å.

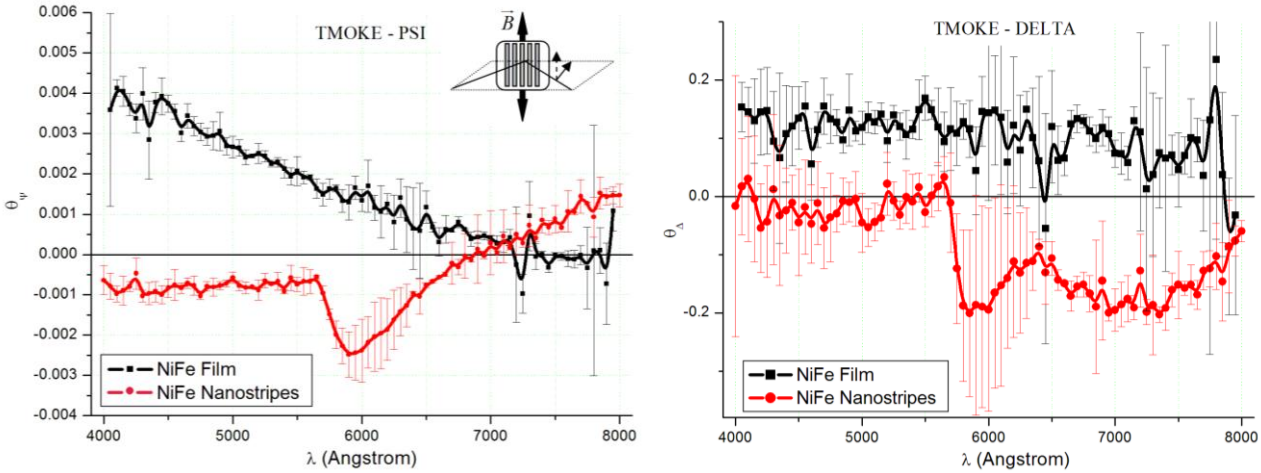

Figure IV.3.3. Transverse MOKE effect measured on a Permalloy nanostripe sample with *d*=377nm compared to plain Permalloy film. Incidence angle is 35 degrees. $\vec{B} = \pm 250$ Oe.

When the MFR spectrum was overlaid on top of the reflectivity spectra (see section IV.2, B), we observed that the TMOKE enhancement peak in fact corresponds to the edge of the Wood Anomaly peak, close to the resonance dip of suspected SPP (Fig. IV.3.4 (a)). In order to confirm the correlation between these phenomena, a Permalloy sample with a different period has been tested (*d*=434 nm). As expected, the TMOKE resonance peak has been observed, with its position shifted to align with the Wood/SPP profiles (Fig. IV.3.4 (b)).

An interesting consequence of changing the period of the structure is observed when the TMOKE spectrum of the second sample (d=434nm) is compared with the spectrum of the Permalloy film. As can be seen in the graph, at the resonance wavelength for the nanostripe sample, the TMOKE effect of plain Permalloy film is very small. As a result the effective enhancement factor in this configuration is about 7.

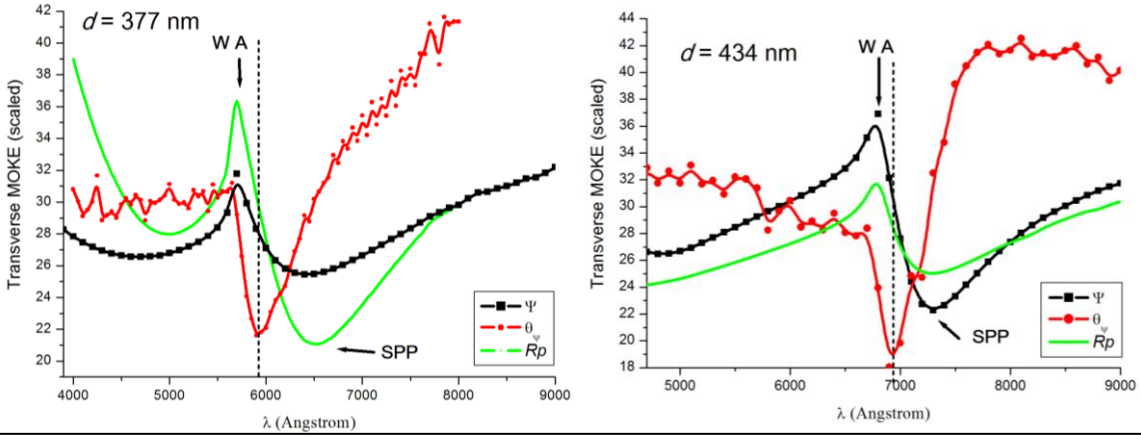

Figure IV.3.4. Transverse MOKE overlaid over ellipsometry and reflectivity spectra for Permalloy nanostripe samples. (a) Stripe period *d*=377nm; (b) *d*=434nm. Arrows show locations of the Wood Anomaly (WA) and of SPP resonances. Dashed line shows the peak of TMOKE enhancement. Angle of incidence is 35degrees. $\vec{B} = \pm 250$ Oe.

The explanation of the TMOKE enhancement phenomenon in periodic magnetic heterostructures has been recently proposed by Belotelov et al. [2009]. Though in their derivation non-magnetic metal slits on a ferromagnetic dielectric substrate was considered, we believe the theory applies to ferromagnetic nanosripes as well.

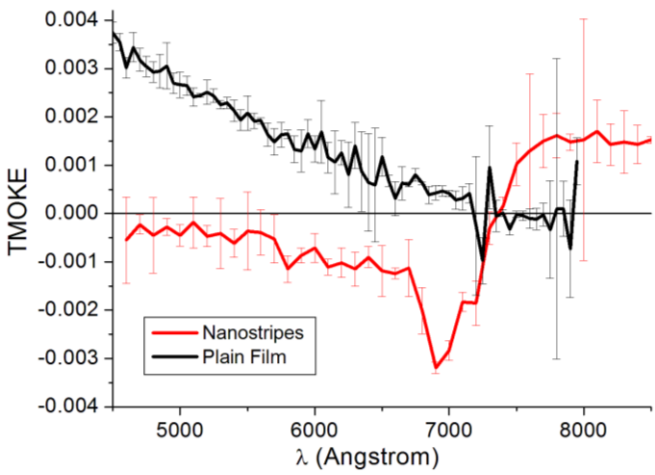

Figure IV.3.5. Transverse MOKE effect measured on a Permalloy nanostripe sample with *d*=434nm compared to the TMOKE effect for a plain Permalloy film. Incidence angle is 35 degrees. $\vec{B} = \pm 250$ Oe.

It is known that in homogeneous plasmonic systems that exhibit transverse Magneto-Optical activity (noble metal/magnetic substrate) the cross product of magnetisation $\vec{m}$ and the surface normal vector $\vec{N}$ is non-zero. This causes a break in spatial and time inversion symmetries. This effect is characteristic of media with a toroidal moment $\vec{\tau}$, whose transformation properties are identical to those of $\vec{m} \times \vec{N}$ [Dubovik et al., 1983]. Thus, propagation of a plasmon-polariton is similar to the propagation of a wave in a medium with a toroidal moment along its direction. Gyration, g, the quantity characteristic of the gyrotropic material is proportional to $\vec{m} \times \vec{N}$ and thus behaves like the toroidal moment.

Analysis of the film surface/dielectric (air) interface shows that the wavenumber of a surface plasmon-polariton propagating along the surface of a *plain* plasmonic film is:

$$k = k_0(1 + \alpha g), \qquad \text{(IV.3.2)}$$

where α is a function of permittivities of the metal and gyrotropic media.

As soon as $\vec{m}$ changes sign, the cross product vector is reflected, manifesting in a change of sign of *g*, resulting in asymmetry of wavevector length. In typical homogeneous structures, the modulus of *g* increases linearly with frequency in the 500-1200nm range. As a result a monotonic TMOKE spectrum is seen.

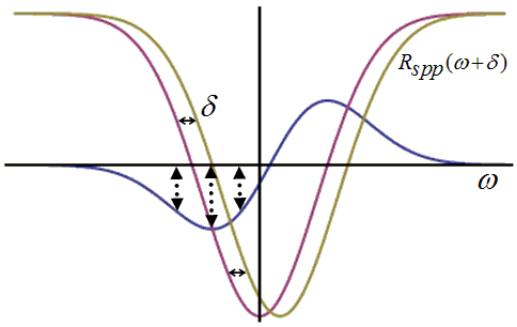

Fugure IV.3.7. Demonstration of the effect of plasmon resonance shift on Transverse MOKE. The Gaussian dip represents the SPP resonant absorption profile in reflection. The asymmetric curve $R_{spp}(\omega+\delta) - R_{spp}(\omega)$ is a proxy for the TMOKE result.

For *periodic arrays of slits*, dielectric and gyrotropic constants are periodic functions. Belotelov et. al [2009] have shown that magneto-optical nonreciprocity also exists for these structures. In this case it affects the frequency of the surface plasmon-polariton. On application of a magnetic field it is shifted by:

$$\Omega(g) = \xi_{n,k} \frac{kg}{\omega_{0n}(k)\varepsilon^2}, \text{ (IV.3.3)}$$

where $\omega_{0n}(k)$ is the SPP frequency for vanishing magnetisation and $\xi_{n,k}$ is a coefficient dependent on the field distribution at the interface. This distribution depends on the grating parameters. A shift in the frequency of the plasmon minimum results in a change in amplitude of the TMOKE effect. The shift of resonances shows up as a maximum of TMOKE when the reflectivity curves for opposite magnetisations are subtracted (Fig. IV.3.7). In general this occurs at the points where the slope of the reflectivity curve is the largest.

Finally, as can be seen from the theory, the enhancement of Transverse MOKE effect requires the presence of a surface plasmon absorption minimum in reflection. This proves that the resonances we saw in reflectivity spectra are Surface Plasmon-Polaritons excited by the Wood's anomaly effect.

C. Bi-Layer noble metal/ferromagnetic metal periodic nanostructures

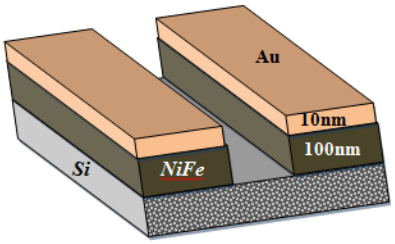

Fugure IV.3.8. Structure of the bi-layer Au/Permalloy nanostripe.

As already seen in sections IV.2.A and IV.2.B, nanostripe arrays made of noble metals (such as Au), exhibit much steeper Wood Anomaly peaks and sharper SPP absorption profiles than those made of Permalloy. Given that the enhancement of the Transverse MOKE effect strongly depends on the gradient of the SPP peak in reflection, it might be advantageous to combine the high magnetic moment of Permalloy and sharper resonance features of Au.

With the view of the above, we have decided to study a bi-layer Au/Permalloy nanostripe structure. The sample in our possession has been manufactured with the same dimensions as the Permalloy nanostripe one, except that on top of the 100nm layer of $Ni_{80}Fe_{20}$ a 10nm capping layer of gold has been added (Fig. IV.3.8).

Measurements of the R_p reflectivity spectrum has shown little difference in the location of diffraction maxima between the pure Permalloy and Au capped nanostripe arrays. Interestingly, though, the surface plasmon profile has now broadened (Fig. IV.3.9). One explanation of this effect is that the layer of gold is thin enough to allow some of the incident light to reach the Permalloy layer. As a result, surface plasmon-polaritons are not only excited on the

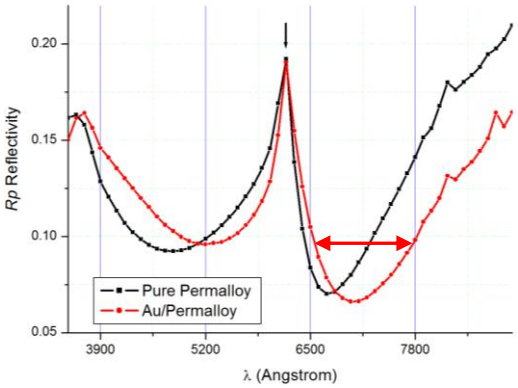

Fugure IV.3.9. Comparison of Rp Reflectivity spectrum of Au Capped Permalloy nanostripes with that of Permalloy only nanostripes. *d*=377nm, angle = 45°.

surface of the sample, but also in the NiFe. Two SPP absorption minima are in relatively close proximity to each other (due to the periodicity of the structure, see Fig.IV.2.10), but do not align precisely because of different ε. A combination of the two minima results in a wider absorption profile.

The broadening of the SPP minimum in the Au/Permalloy reflectivity spectrum is accompanied in the reduction of the gradient of the curve. From theory one can see that this should result in decrease in magnitude of the TMOKE effect. This indicated that a high gain in the magneto-optical effect is not likely to be achieved as a result of addition of a thin Au capping layer. MFR ellipsometric spectroscopy has indeed confirmed that the TMOKE resonance is slightly damped (Fig.IV.3.10) and broadened in comparison to the case of pure Permalloy.

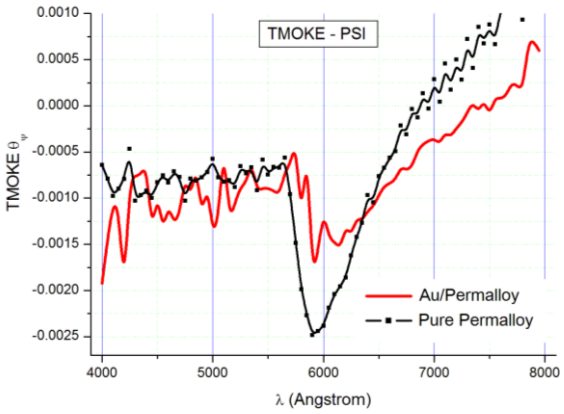

Fugure IV.3.10. Comparison of TMOKE spectrum of Au Capped Permalloy nanostripes with that of Permalloy only nanostripes. *d*=377nm, angle = 35°.

V. Conclusions and outlook

In this project we have investigated properties of plasmonic excitations that occur in thin magnetic films and nanostructures. The following conclusions can be made as a result of this work:

1. Comparison of optical pseudo-dielectric Loss Function and Electron Energy Loss spectra of thin films of Ag metal have revealed that multiple surface plasmon and hybrid resonances can occur in the spectral range of light of 320-350 nm (3.65-3.75 eV). These resonances can be excited directly by electron scattering or optically by coupling the moments and energies of incident photons to plasmon frequencies by surface and volume roughness.
2. Studies of periodic nanostructures using a Variable Angle Spectroscopic Ellipsometer (VASE) have shown that:
    a) Their optical response strongly depends on the polarization of incident light;
    b) Surface plasmon-polaritons in these structures can only be excited when light is scattered into the 1st order of diffraction and the diffracted beam propagates at grazing angles with the nanostripe plane;
    c) Positions of resonances depend on the incidence angle and the nanostructure period, as well as on the dielectric function of the material.
3. By upgrading VASE to include the option of magnetic field-resolved ellipsometry, effects of magnetic fields on surface plasmon-polaritons and the overall magneto-optical response of nanostructured systems can be investigated.
4. Surface plasmon-assisted enhancement of Transverse MOKE is present in arrays of ferromagnetic nanostripes. The gain in TMOKE response strongly depends on magnetic and dielectric properties of the materials.

The knowledge acquired during the work on this project opens up thrilling prospects for future plasmonic and magneto-plasmonic research at CAMSP. Further experimental and theoretical analysis of nanostripe arrays and improvements to multi-layer structures with a prospect of enhancing resonance effects will be considered as a result of this effort.

Furthermore, possible further experiments include non-destructive electron spectroscopic analysis of the periodic nanostructures, such as spin-polarized EELS. In that framework an extension of electron scattering methods to optical detection of plasmon decay would be of great interest.

Also it will be advantageous to study the magnetic nanostructures in transmission. Similar to the materials studied by Belotelov et al.(2009) one may expect dependence of the anomalous transmission by nanoslits or nanovoids on the applied field for these structures. To enable these measurements the magnetic nanostripe, anti-dot and nanovoid arrays should be fabricated on transparent substrates such as quartz. The DUV lithography at the National University of Singapore is compatible with this type of substrates.

VI. References

1. Adeyeye A.O., Singh, N., *J. Phys. D* **41** (153001).
2. Andrew, P., Barnes, W. L., 2004, Science **306** (1002).
3. Belotelov, V.I., Akimov, I.A., Pohl, M., Kotov, V.A., Kasture S., Vengurlekar, A.S., A.V. Gopal, D.R. Yakovlev, A.K. Zvezdin, M. Bayer, 2011, Nature Nanotech. **6** (370).
4. Belotelov, V.I., Bykov, D.A., Doskolovich, L.L, Kalish, N.A, Zvezdin, A.K., 2009, *JOSA B* **26** (8).
5. Charbonneau, R., Berini, P., Berolo, E., Lisicka-Shrzek, E., 2000, *Opt. Lett.* **25** (844).
6. Dubovik, V.M., Tosunyan, L.A., 1983, *Fiz. Elem. Chastits At.Yadra* 15 (1193).
7. Ebbesen, T. W., Lezec, H. J., Ghaemi, H. F., Thio, T., Wolff, P. A., 1998, *Nature* **391** (6668).
8. Fujiwara, H., Spectroscopic Ellipsometry: Principles and Applications, 2007, Wiley.
9. Gippius N.A., Tikhodeev, S.G., Christ, A., Kuel, J., Gissen, H., 2005, *Phys. Sol. State* **47** (1).
10. Gramotnev, D.K., Bozhevolnyi, S.I., 2010, *Nature Photon*. **4** (83).
11. Grunin A.A., Zhdanov, A.G., Ezhov, A.A., Ganshina E.A, Fedyanin, A.A., 2010, *Appl. Phys. Lett.* **97** (261908)
12. Heenan, E., *Spectroscopic ellipsometric characterisation of optical properties of thin films*, Honours Thesis, UWA, 1998.
13. Ibach, H., 1991, *'Electron Energy Loss Spectrometers – The Technology of High Performance'*, Springer-Verlag.
14. Ibach, H., Lüth, H., *Solid-State Physics: An Introduction to Principles of Materials Science*, 2010, Springer-Verlag, New York.
15. Jasperson, S.N., Schnatterly S.E., 1969, *Phys. Rev.* **188** (1).
16. Kittel C., *Introduction to solid state physics*, 1986, John Wiley & Sons.
17. Knill, E., 2010, *Nature* **463** (441).
18. Kokogawa, T., Numata, T., Inokuchi, S., 1993, *IEEE Trans. Mag.* **29** (6).
19. Komolov, S.A., *Total Current Spectroscopy of Surfaces*, 1992, Gordon and Breach Science Publishers.
20. Kostylev, M., Stashkevich, A.A., Adeyeye, A.O., Shakespeare, C., Kostylev, N., Ross, N., Kennewell, K., Magaraggia, R., Roussigné, Y., Stamps, R.L., 2010, *J. Appl. Phys.* **108** (103914).
21. Krasavin, A.V., Zheludev, N.I., 2004, *Appl. Phys. Lett.* **84** (1416).
22. Krasavin, A.V., Zayats, A.V., Zheludev, N.I., 2005, J. Opt. A: Pure Appl. Opt. **7** (S85).
23. Kravets, V. G., Schedin, F., Grigorenko A. N., 2008, *Phys. Rev. Lett.* **78** (205405).
24. Kravets, V.G., Schedin, F., Grigorenko, A.N., 2008, *Phys. Rev. B* **78** (205405).
25. Krenn, J. R., Weeber, J.C., 2004, *Philos. Trans. R. Soc. Lond. Ser. A* **362** (739).
26. Lamprecht, B., Krenn, J. R., Schider, G., Ditlbacher, H., Salerno, M., Felid, J.N., Leitner, A., Aussenegg F.R., Weeber, J.C., 2001, *Appl. Phys. Lett.* **79** (51).
27. Larkin, I.A., Stockman, M.I., Achermann, M, Klimov, V.I., 2004, *Phys.Rev. B* **69** (121403).
28. Liebsch, A., 1985, *Phys. Rev. Lett.*, **54** (67).

29. Lord Rayleigh, 1907, *Proc. R. Soc*. A **79** (399).
30. Maier, S.A., *Plasmonics: Fundamentals and Applications,* 2007, Springer-Verlag, New York.
31. Nakayama, H., Nishino, T., Ueda, K., Takeno, S., and H. Fujita, 1991, *Ultramicroscopy* **39**.
32. Nikolajsen, T., Leosson, K., Salakhutdinov, I., Bozhevolnyi, S.I., 2003, *Appl. Phys. Lett.*, **82** (668).
33. Ozbay, E., 2006, *Science* **311** (5758).
34. Penfold C., Collins R.T, Tufaile A.P.B., 2002, Souche Y., J. Magn. Magn. Mater. **242** (2).
35. Peruzzo, A., Laing, A., Politi, A., Rudolph, T., O'brien, J.L., 2010, *Nature Comm.* **2** (224).
36. Pines, D., Bohm, D, 1952, *Phys. Rev.* **85** (338).
37. Powell, C. J., Swan J. B., 1959, *Phys. Rev.* **115** (869).
38. Prasad, P.N., *Nanophotonics*, 2004, Wiley.
39. Pulisciano A., Park, S.J., Palmer R.E., 2008, *Appl. Phys. Lett.*, **93** (21).
40. Raether, H. , *Surface plasmons on smooth and rough surfaces and on gratings,* 1988, Springer-Verlag, Berlin, Heidelberg, New York
41. Ritchie, R.H., 1957, *Phys Rev*. **106** (874).
42. Ritchie, R.H., 1957, *Phys. Rev*. **106** (874).
43. Robins J. L., Swan, J. B., 1960 *Proc. Phys. Soc.* **76** (857).
44. Rocca, M., Biggio, F., Valbusa, U., 1990, *Phys. Rev. B* **42** (5).
45. Ross, M., Oskin, M., 2008, *Comm. ACM* **51** (7).
46. Ruthemann, G.,1948, *Ann. Phys.* **2** (113).
47. Safarov, V.I., Kosobukin, V. A., Hermann, C., Lampel, G. Peretti, J., 1994, *Phys. Rev. Lett.* **73** (3584).
48. Samarin, S.N., Artamonov, O.M., Waterhouse, D.K., Kirschner, J., Morozov, A., Williams, J.F., 2003, *Rev. Sci. Instr.* **74** (3).
49. Sokolov, A.V., *Optical Properties of Metals,* 1967, Blackie and Son, London.
50. Steel, M.R., *JOSA* **63** (1).
51. Taneja, P., Ayyub, P., Chandra, R., 2002, *Phys. Rev. B* **65** (24).
52. Temnov, V., Armelles, G., Woggon, U., Guzatov, D., Cebollada, A., Garcia-Martin, A., Garcia-Martin, J-M., Thomay, T., Leitenstorfer, A., Bratschitsch, R., 2010, *Nature Photon.***4** (107).
53. *VASE Hardware Manual*, 1996, J.A. Woolam Co. Inc., Lincoln, USA.
54. Vyalykh, D.V., Shikin, A.M., Prudnikova, G.V., Grigor'ev, A.Y., Starodubov, A.G., Adamchuk, V.K., 2001, *Phys. Sol. State* **44** (1).
55. Wood, R.W., 1902, *Philos. Mag*. **4** (396).
56. Wurtz, G. A. et al., 2008, *New J. Phys.* **10** (105012).
57. Zvezdin, A.K., Kotov, V.A., *Modern magneto-optics and magnetooptical materials*, 1997, Institute of Physics, Bristol.

Appendix A

Bulk & surface plasmon theory

Many of the fundamental electronic properties of the solid state can be successfully described by the analogy of single electrons moving in a periodic array of atoms. A somewhat different approach is to derive the properties of the solid state is to consider the plasma concept: the free electrons of a metal are treated as an electron liquid of high density (Raether, 1988). This approach was further developed by Pines and Bohm in the 1950s (Pines and Bohm, 1952) in order to explain the phenomena of energy losses in fast electron scattering experiments (Rutheman, 1948). They have shown that the long-range nature of the Coulomb interaction between the sea of valence electron in metals yield collective volume plasma oscillations similar to the electron-density oscillations observed in electrical discharges in gases.

A *plasmon* is defined as a quantum of a plasma oscillation. A plasma oscillation in a bulk of a metal is a collective longitudinal excitation (see Fig. II.1.1) of the conduction electron gas. The quantum of this oscillation has an energy:

$$\hbar\omega_p = \hbar\sqrt{\frac{4\pi ne^2}{m_e}}, \quad \text{(II.1.1)}$$

where *e* is the charge of an electron, m_e is its mass, *n* is the electron density, and ω_p is the bulk plasmon frequency.

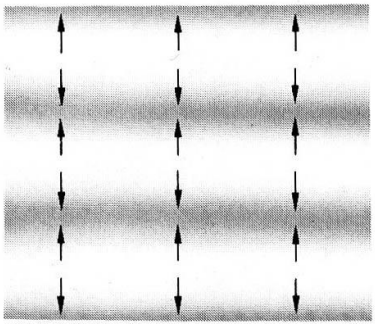

Figure II.1.1. Free longitudinal plasma oscillation. The arrows indicate the direction of displacement of the electrons. [Kittel, p261, fig4]

The dielectric function $\varepsilon(\omega,\vec{k})$ of a crystal, used to describe its response to an electromagnetic field, contains a strong dependency on frequency and wave vector of incident radiation. This has significant consequences for the physical properties of the solid. In one of its limits, $\varepsilon(\omega,0)$, it is used (Kittel, 1986) to define the conditions for existence of plasmons in matter. The *bulk plasmons* can only be excited in a medium at frequency ω_p, for which the following condition is satisfied

$$\varepsilon(\omega) = 1 - \frac{{\omega_p}^2}{\omega^2}. \quad \text{(II.1.2)}$$

A more detailed derivation of formulae in this section can be found in the Appendix. The relationship (II.1.2) is plotted in Fig. II.1.2.

The effects of condition (II.1.2) are easily understood when the dispersion relation of electromagnetic waves is considered:

$$\varepsilon(\omega,\vec{k})\varepsilon_0\mu_0\omega^2 = k^2. \quad \text{(II.1.3)}$$

When $\varepsilon(\omega)$ is negative[1], i.e. $\omega < \omega_p$, k is complex and the electromagnetic wave $E \propto e^{-i\omega t} e^{i(\vec{k}\cdot\vec{r})}$ is damped in space with characteristic length $1/|k|$. On the other hand, at $\omega > \omega_p$, the permittivity of the material becomes real positive. This means that k is real and a transverse electromagnetic wave can propagate through the material with phase velocity $c/\sqrt{\varepsilon}$. In essence, the material becomes transparent to light at these frequencies.

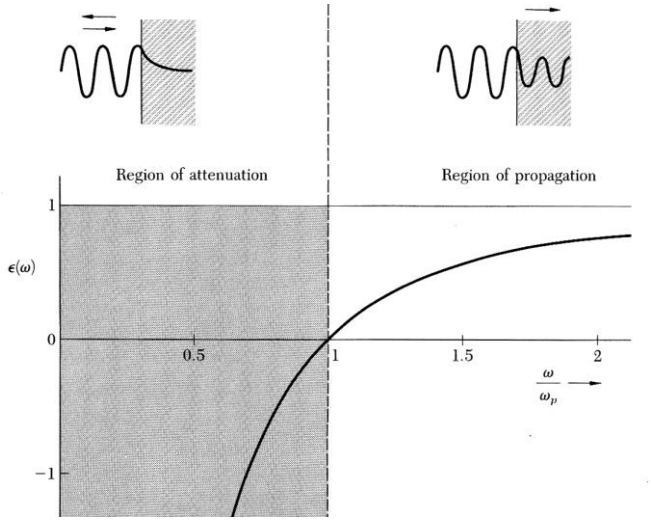

Figure II.1.2 Dielectric function of free electron gas versus frequency in units of plasma frequency. Bulk plasmon are excited when $\omega/\omega_p = 1$. Above that frequency the material is transparent. Image: [Kittel, p254].

Excitation plasmons is not only limited to the bulk of a material. The surface of a solid, which is commonly referred to as a thin film or a thin (mono)layer (Werner, 1984), is usually modelled as an infinitely thin gas-solid interface. It has been first shown by Ritchie (1957) that plasmons can also exist at this boundary. Coherent electron oscillations that exist at the interface between any two materials (Fig. II.1.3), typically between a metal and a dielectric, are known as *surface plasmons* (SPs).

In order to represent surface plasmons, the original argument must be adopted to include the continuity and boundary conditions that exist at the two-material interface. The electric field propagating along a surface can be expressed as (Raether, 1988):

$$E = E_0^{\pm} e^{i(k_x x \pm k_z z - \omega t)}, \qquad \text{(II.1.4)}$$

where $\vec{K} = k_x\hat{x} + k_z\hat{z}$ is the propagation wavevector. The *z*-coordinate is chosen to represent the depth of penetration into the film and *x* is along the surface. The amplitude of *E* decreases with $|z| \to \infty$ (Fig. II.1.4), with the maximum being located at *z* = 0. This means that the waves are localized primarily in the surface, with the field E_z decaying exponentially fast outside the surface bounds.

Maxwell's equation yield the retarded dispersion relation for the plane surface of a semi-infinite metal with the complex dielectric function ($\varepsilon_I = \varepsilon_I' + i\varepsilon_I''$), adjacent to a medium ε_{II}, such as air or vacuum (Raether, 1988). With the wave vector $\vec{k_x}$ continuous through the interface, the dispersion relation in the *x*-direction can be written as:

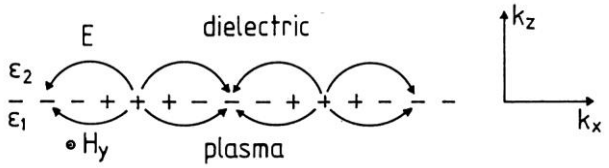

Figure II.1.3. Schematic representation of the charges and the electromagnetic field of SPs propagating in the *x*-direction. H_y shows the magnetic field in the *y*-direction of the *p*-polarized SP wave. (Raether, 1988)

$$k_x = \frac{\omega}{c}\left(\frac{\varepsilon_I \varepsilon_{II}}{\varepsilon_I + \varepsilon_{II}}\right)^{1/2}. \qquad \text{(II.1.5)}$$

[1] For simplicity, in this analysis only the case of real ε is considered. Complex permittivity will, in general, result in damping of the wave.

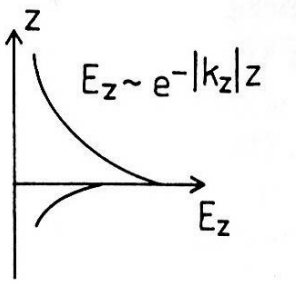

Figure II.1.4. The exponential dependence of E_z of a surface-propagating plasmon.

Assuming $\omega \in \mathbb{R}$, $\varepsilon_2 \in \mathbb{R}$ (good dielectric), and $\varepsilon_I'' < |\varepsilon_I'|$, from Eqn. (II.1.5) it can be deduced that k_x is complex:

$$k_x = k_x' + ik_x''$$

$$k_x' = \frac{\omega}{c}\sqrt{\frac{\varepsilon_I'\varepsilon_{II}}{\varepsilon_I' + \varepsilon_{II}}} \quad . \qquad \text{(II.1.6)}$$

$$k_x'' = \frac{\omega}{c}\left(\frac{\varepsilon_I'\varepsilon_{II}}{\varepsilon_I' + \varepsilon_{II}}\right)^{3/2} \frac{\varepsilon_I''}{2(\varepsilon_I')^2}$$

The resulting dispersion relation is shown in Fig. II.1.5. At small k_x the relation approaches the light line $\sqrt{\varepsilon_{II}}\frac{\omega}{c}$, but never crosses it. In that regime the excitation cannot be transformed into photons, meaning that the surface plasmon is of a nonradiative nature.

At large k_x, $\varepsilon_I' \to -\varepsilon_{II}$, which means that the surface plasmon frequency is given by

$$\omega_{sp} = \frac{\omega_p}{\sqrt{1+\varepsilon_{II}}}, \qquad \text{(II.1.7)}$$

with ω_p defied above in Eqn. (II.1.2). In the case of air ($\varepsilon_{II} = 1$), the expression simplifies to:

$$\omega_{sp} = \frac{\omega_p}{\sqrt{2}}. \quad \text{(II.1.8)}$$

In the case of a large k_x the group and phase velocities approach zero, with the implication that the SP resembles a surface localized fluctuation of the electron plasma.

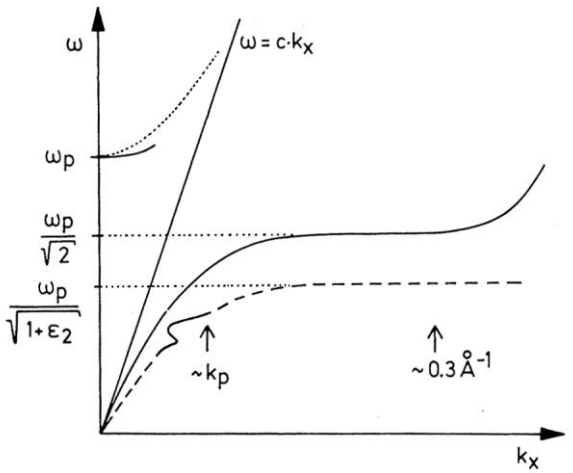

Figure II.1.5. Dispersion relation of surface plasmons. Light line: $\omega = ck_x$. Continuous curve: nonradiative SPs (right) and radiative SPs (left).

Dashed line: SPs on a metal surface coated with dielectric (ε_{II}) film. (Raether, 1988)

Appendix B

DAC Control Box

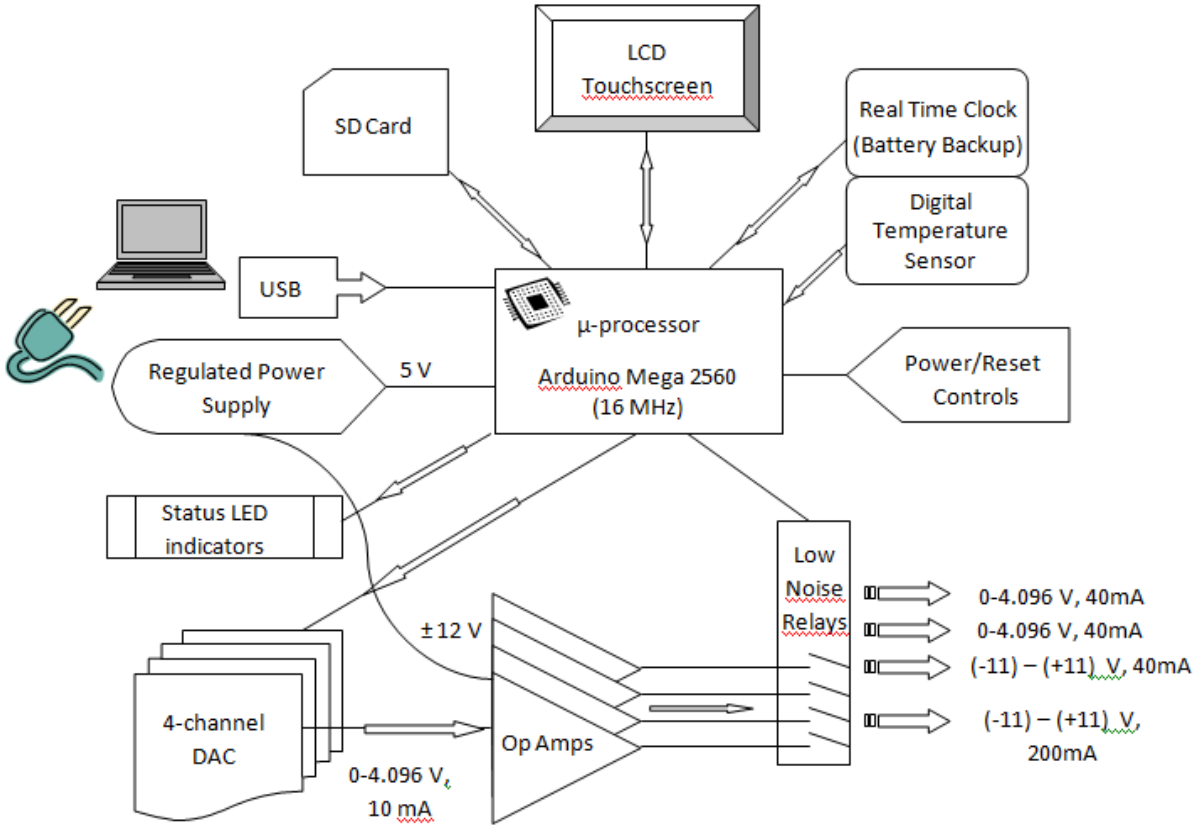

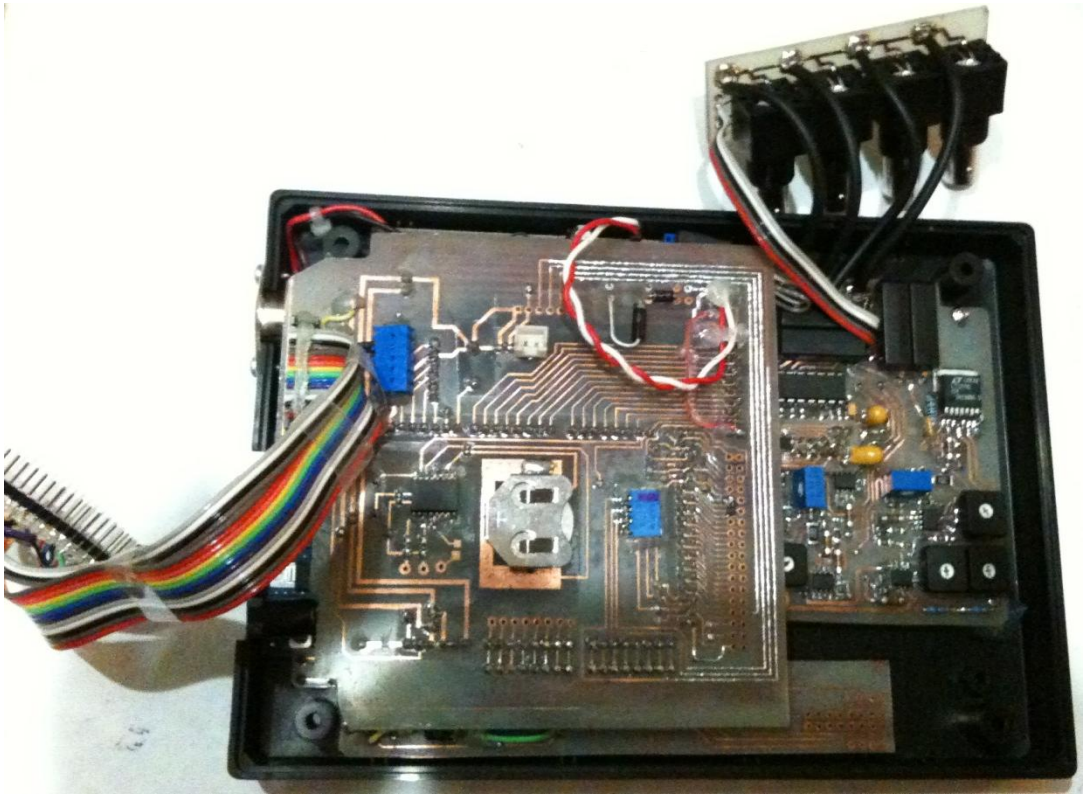

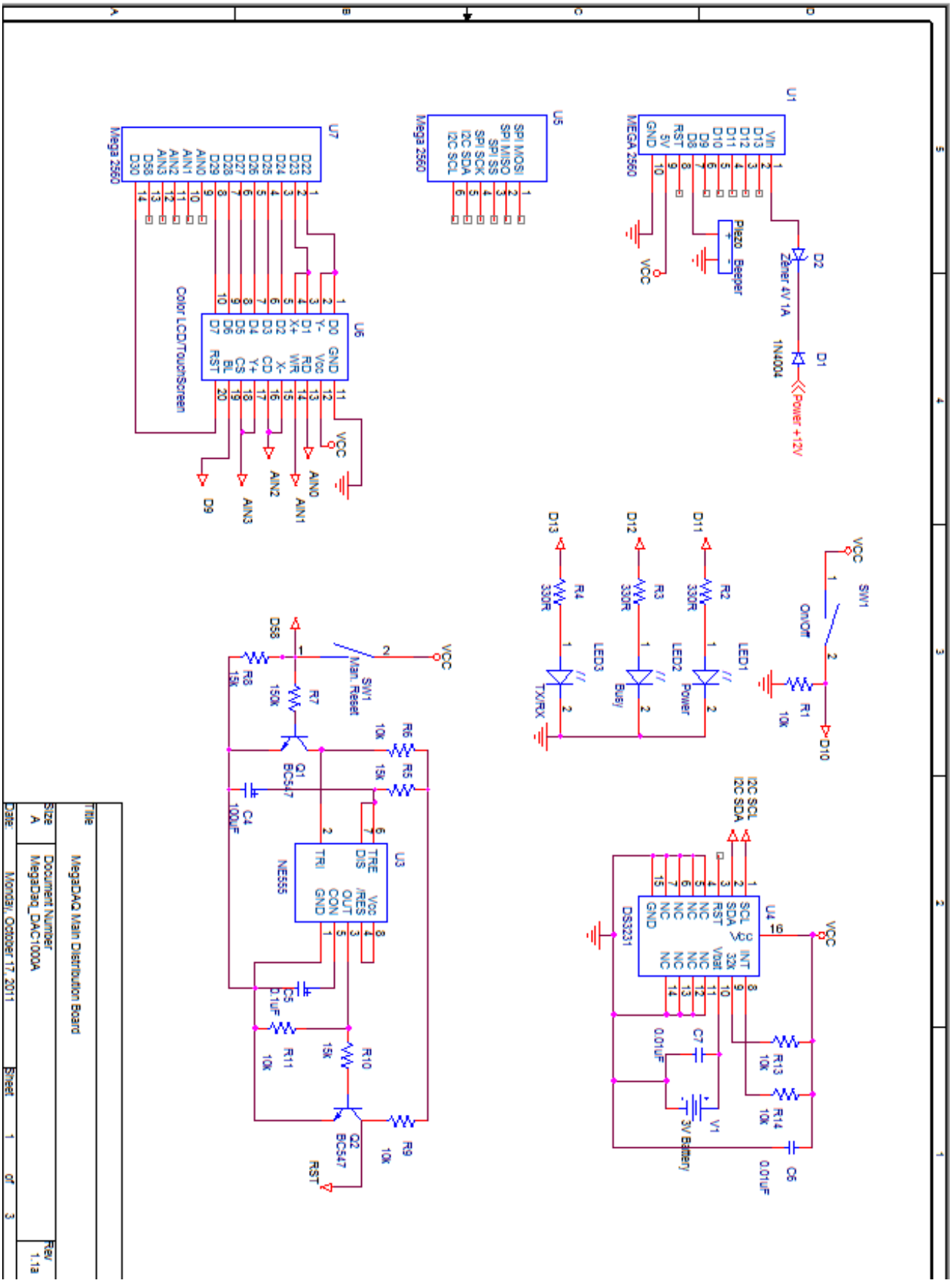
MegaDAQ Main Distribution Board
Document Number
MegaDaq_DAC1000A
Rev
1.1a
Monday, October 17, 2011
Sheet 1 of 3
Size A
Date
Title
Power +12V
1N4004
2Amp 4V 1A
Piezo_Beeper
Mega 2560
Color LCD/TouchScreen
On/Off
Man. Reset
TX/RX
Busy
Power
DS3231
3V Battery
NE555
BC547
330R
10k
15k
150k
100uF
0.1uF
0.01uF
32k
I2C SCL
I2C SDA
RST
VCC
GND

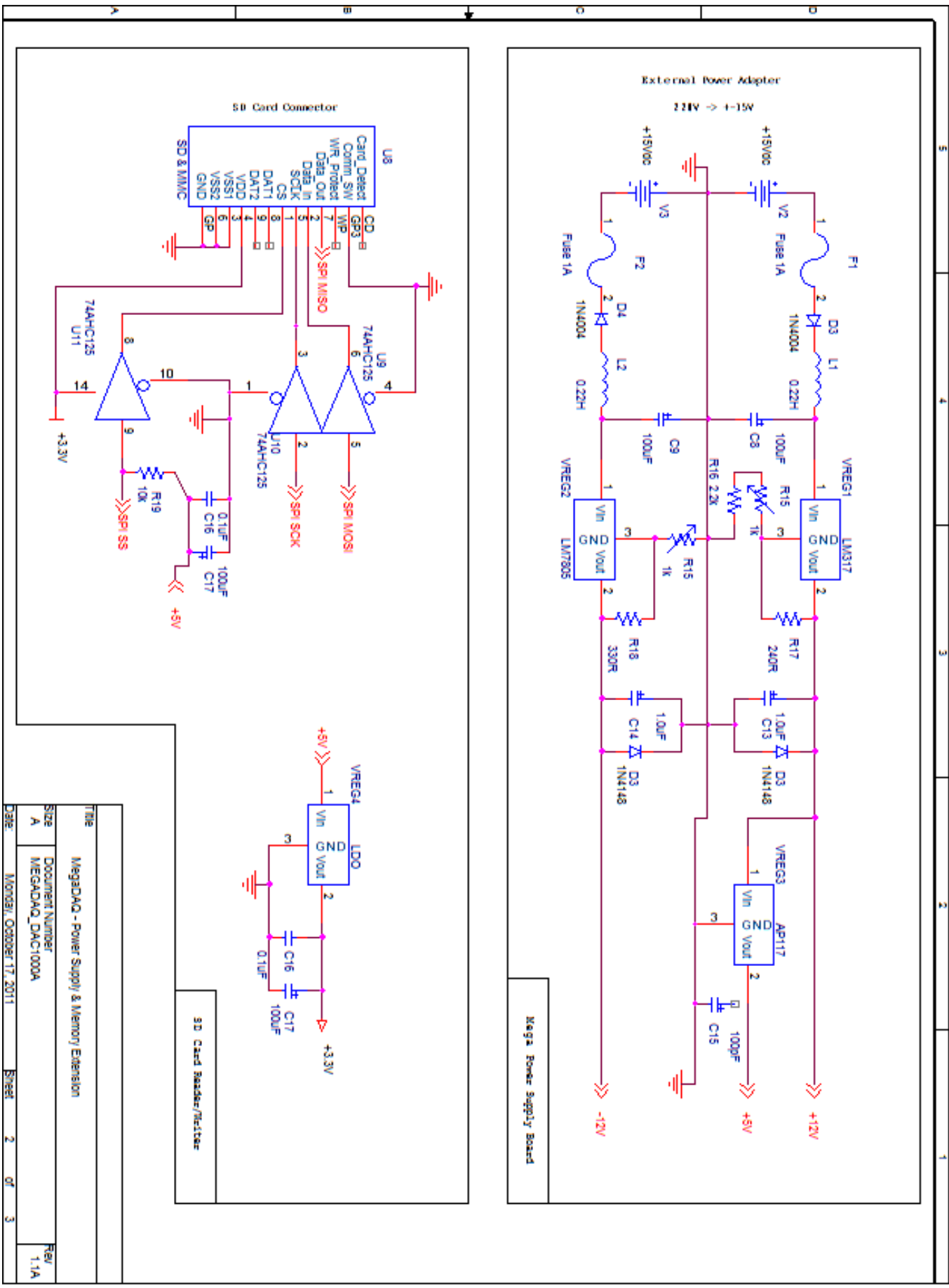
External Power Adapter
220V -> +-15V
+15Vdc
+15Vdc
V3
V2
Fuse 1A
Fuse 1A
F2
F1
1N4004
D4
D3
1N4004
L2
L1
0.22H
0.22H
C9
100uF
C8
100uF
R16 2.2k
R15
1k
VREG2
LM7805
Vin
GND
Vout
VREG1
LM317
Vin
GND
Vout
R15
1k
R18
330R
R17
240R
1.0uF
C14
1.0uF
C13
D3
1N4148
D3
1N4148
VREG3
AP117
Vin
GND
Vout
C15
100pF
-12V
+5V
+12V
Mega Power Supply Board
SD Card Connector
U8
Card_Detect
Comm_SW
WR_Protect
Data_Out
Data_In
SCLK
CS
DAT1
DAT2
VDD
VSS1
VSS2
GND
SD & MMC
CD
GP3
WP
GP
SPI MISO
74AHC125
U11
U9
74AHC125
U10
74AHC125
+3.3V
R19
10k
0.1uF
C16
100uF
C17
SPI SS
SPI SCK
SPI MOSI
+5V
+5V
VREG4
LDO
Vin
GND
Vout
C16
0.1uF
C17
100uF
+3.3V
SD Card Reader/Writer
Title
MegaDAQ - Power Supply & Memory Extension
Size
A
Document Number
MEGADAQ_DAC1000A
Rev
1.1A
Date:
Monday, October 17, 2011
Sheet
2
of
3

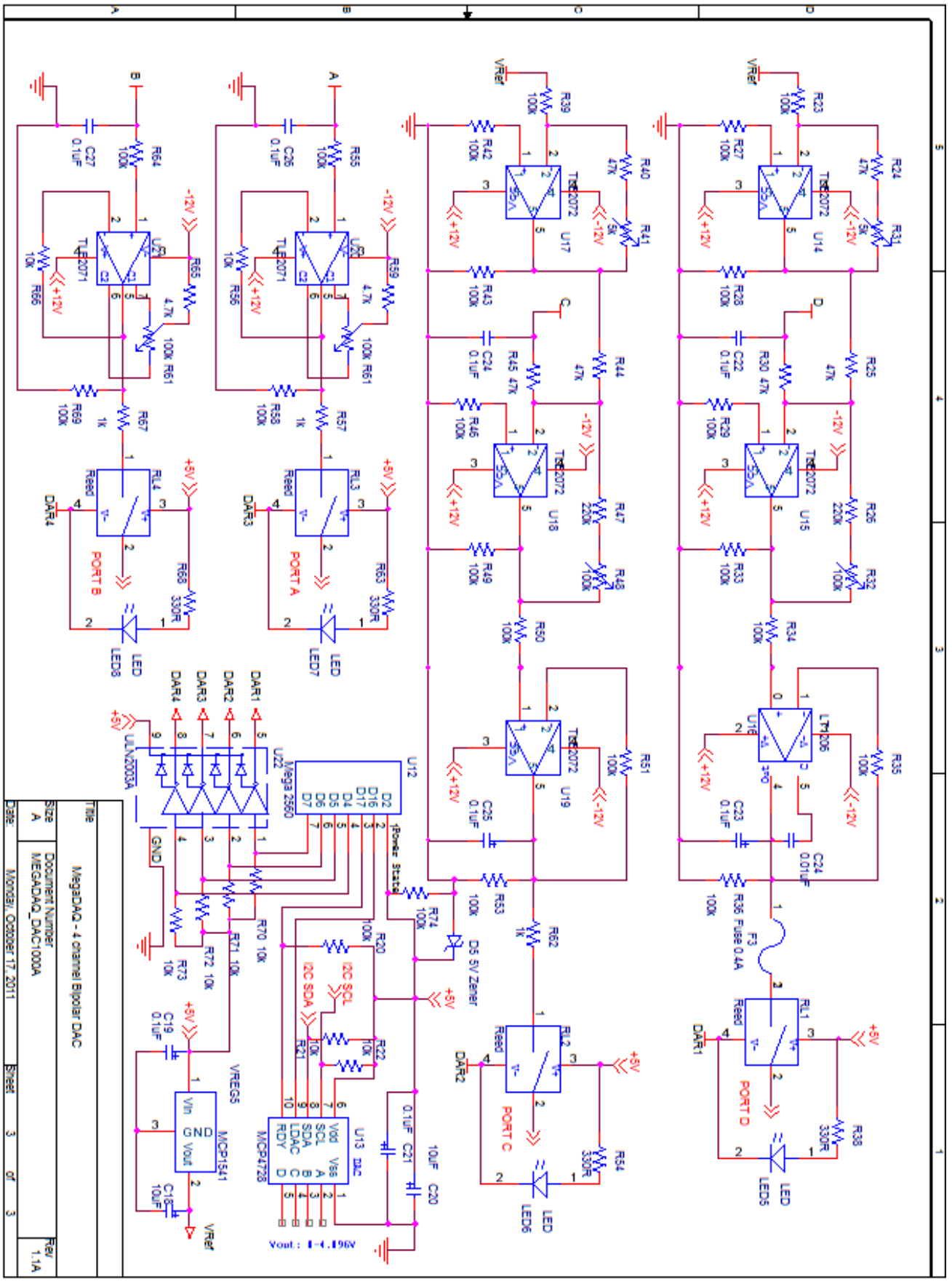
MegaDAQ - 4 channel Bipolar DAC
MEGADAQ_DAC1000A
Monday, October 17, 2011
1.1A

Appendix C
Software

These are the screenshots of the software I have written. The code is available by request. All of the software has been written in Borland Delphi 7.

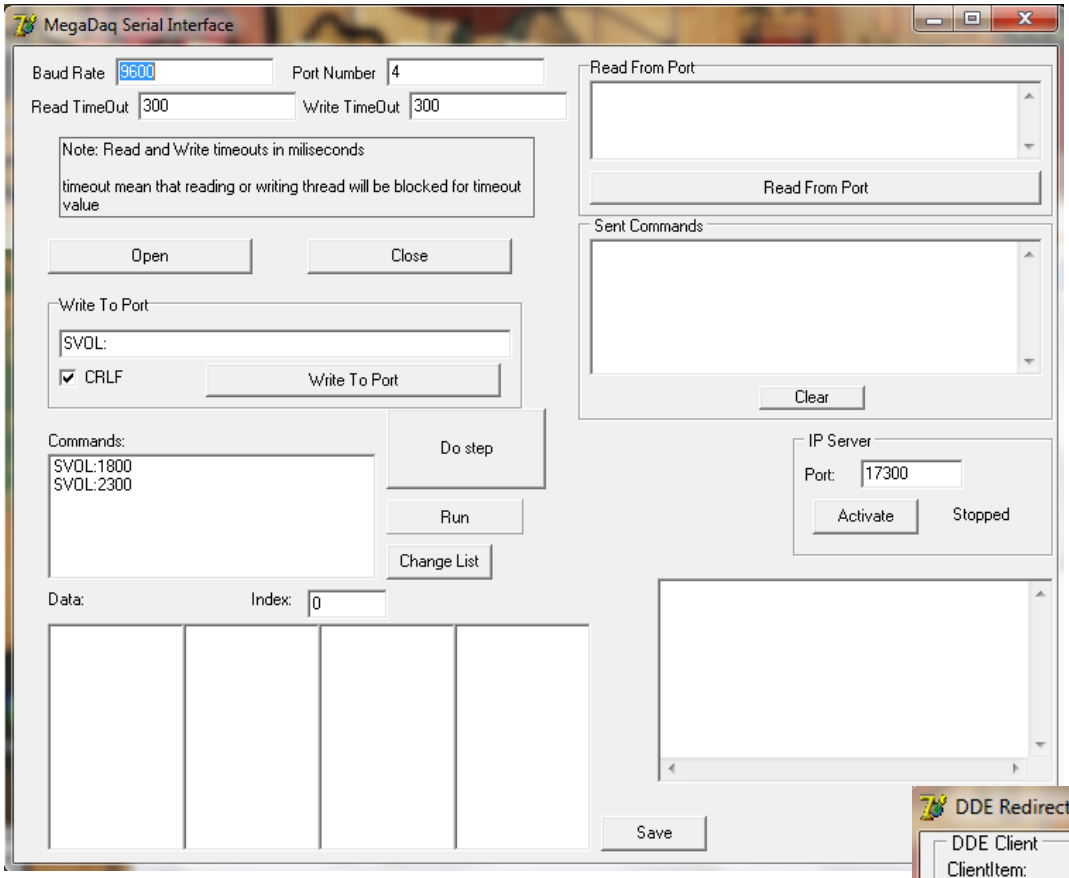

< This application was used to receive ellipsometer data sent over the network and control the DAC via the serial port.

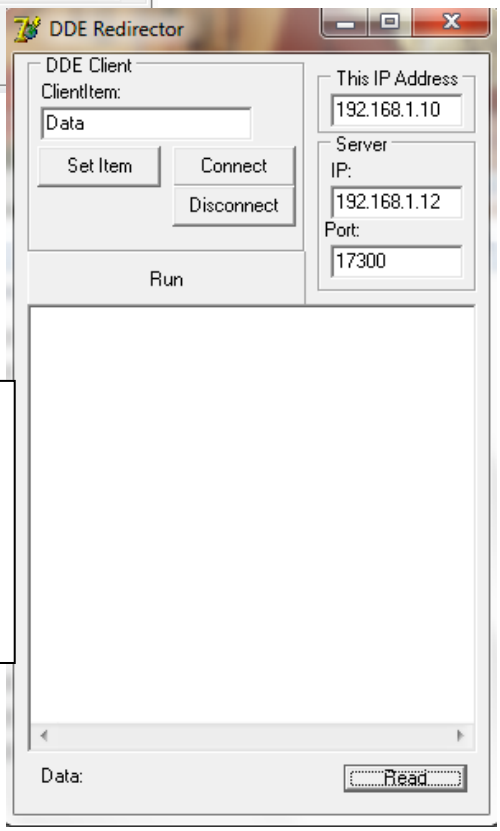

>

This application received data from the ellipsometer software via the DDE Protocol and sent it over the network to the program above.

Appendix D

Ag/Si thin film sample: refractive index fit

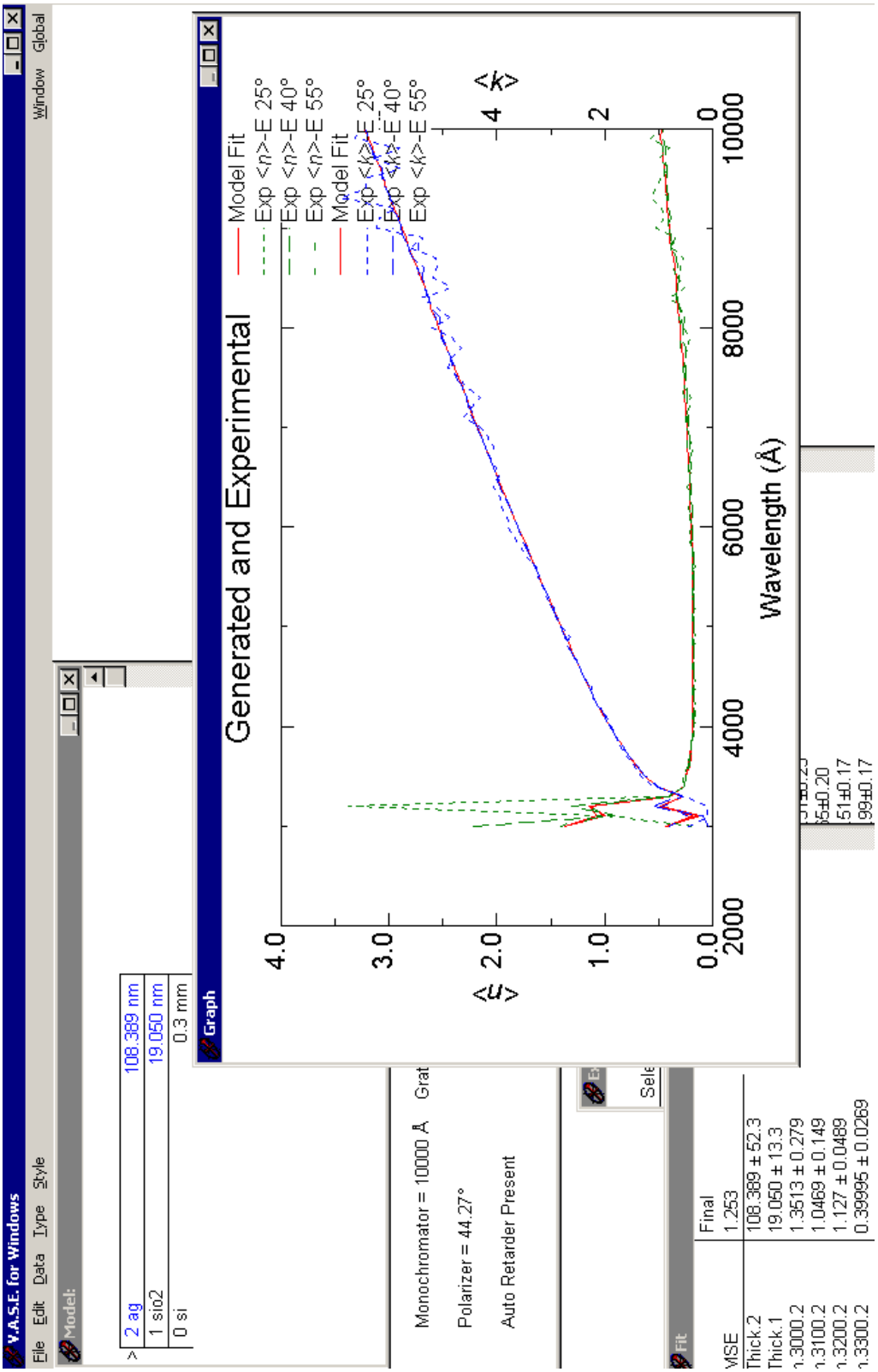

Appendix E

Pseudo-dielectric function of silver (measured at 35 degrees incidence)

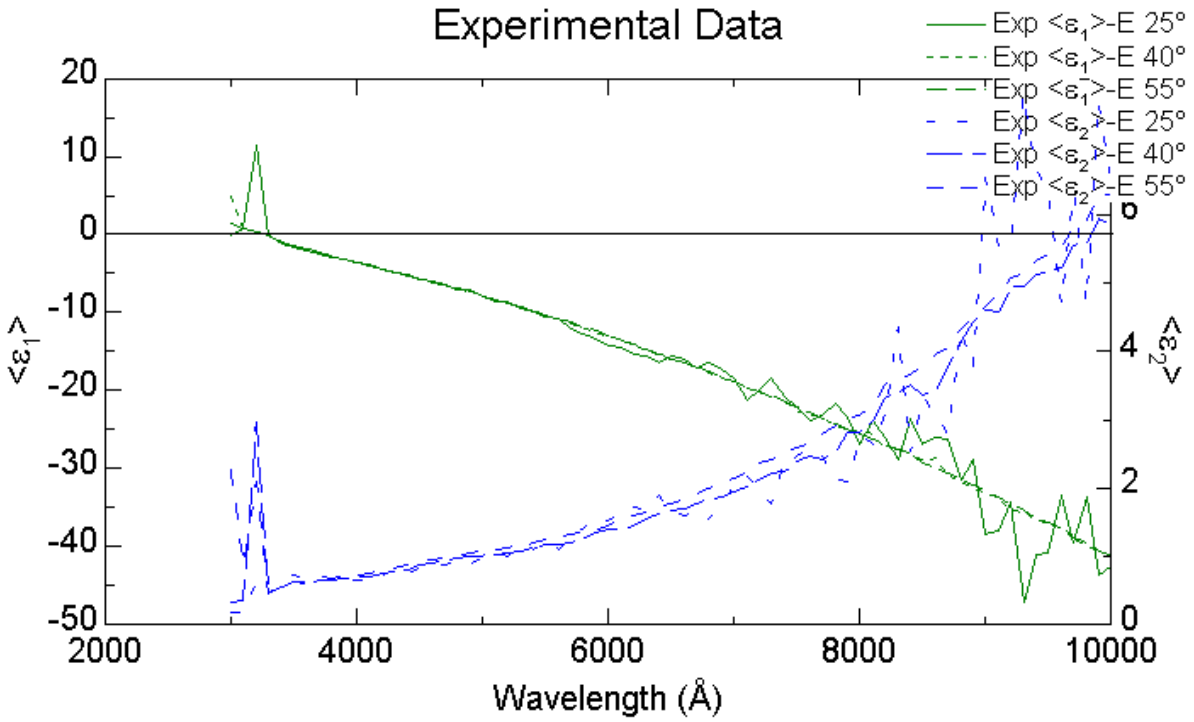

Appendix F

Measurement geometries used for recording reflectivity and ellipsometry spectra of nanostripes

The following graphs show the positioning of the samples and magnetic field relative to the plane of incidence of the light beam inside the VASE ellipsometer setup. In cases, where plain films were used as samples, "Horizontal" and "Vertical" arrangements are equivalent.

Ψ and Δ ellipsometric parameters

Stripes' orientation: "**HORIZONTAL**" (Parallel to plane of incidence)

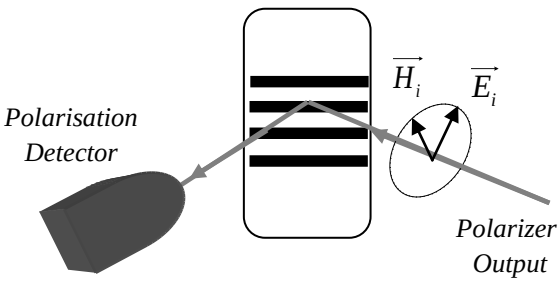

Ψ / Δ **Measurement**: incident light polarized automatically (≈45°)

Stripes' orientation: "**VERTICAL**" (Perpendicular to plane of incidence)

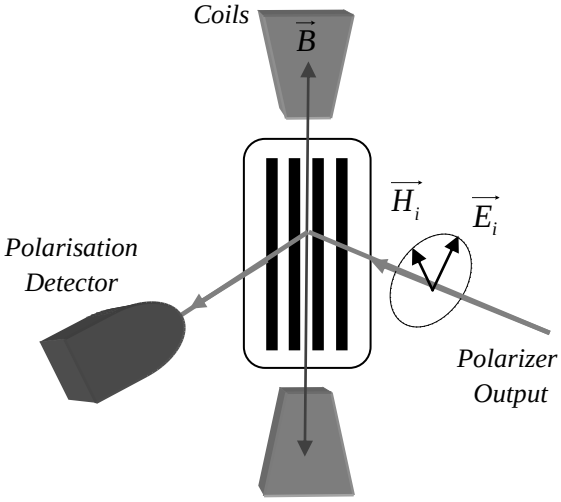

Ψ / Δ **Measurement**: incident light polarized automatically (≈45°)

Note: during standard ellipsometric measurements of Ψ / Δ parameters, the magnetic field was not used. Coil windings producing a transverse magnetic field, shown on the above two graphs, have been attached only for TMOKE measurements. Kerr Rotation was successfully detected only in the Ψ / Δ "Vertical" arrangement.

Reflection of p- and s-polarized light

Stripes' orientation: "**HORIZONTAL**"
(Parallel to plane of incidence)

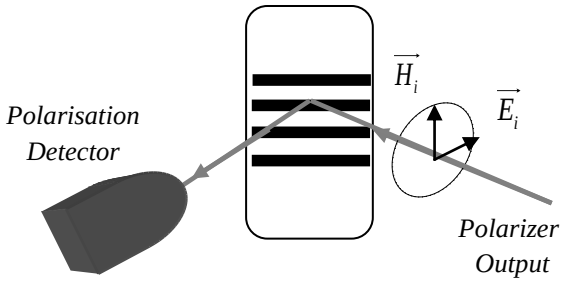

***pR* Measurement**: incident light *p*-polarized
($\vec{E}_i$ parallel to stripes)

Stripes' orientation: "**VERTICAL**"
(Perpendicular to plane of incidence)

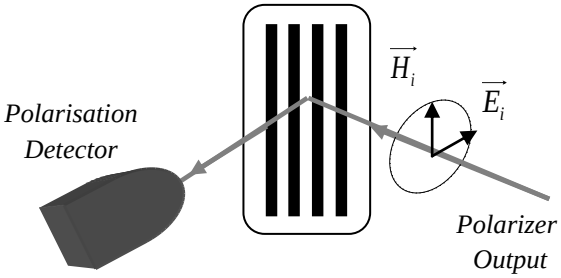

***pR* Measurement**: incident light *p*-polarized
($\vec{E}_i$ perpendicular to stripes)

Stripes' orientation: "**HORIZONTAL**"
(Parallel to plane of incidence)

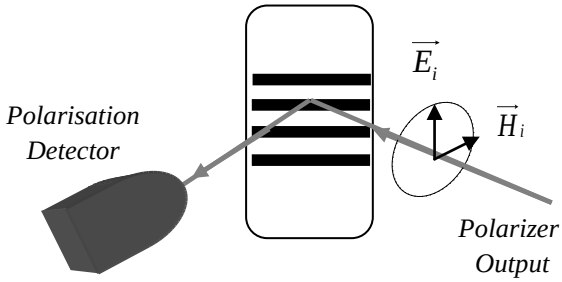

***sR* Measurement**: incident light *s*-polarized
($\vec{E}_i$ perpendicular to stripes)

Stripes' orientation: "**VERTICAL**"
(Perpendicular to plane of incidence)

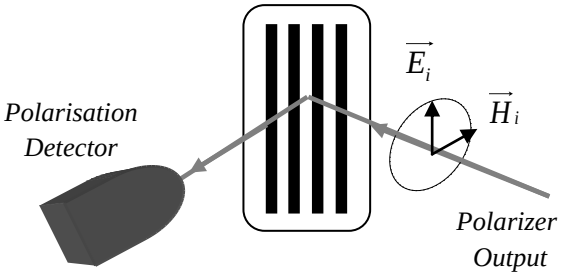

***sR* Measurement**: incident light *s*-polarized
($\vec{E}_i$ parallel to stripes)

Appendix G

Pseudo-dielectric functions of Au and Permalloy (measured at 35 degrees incidence)

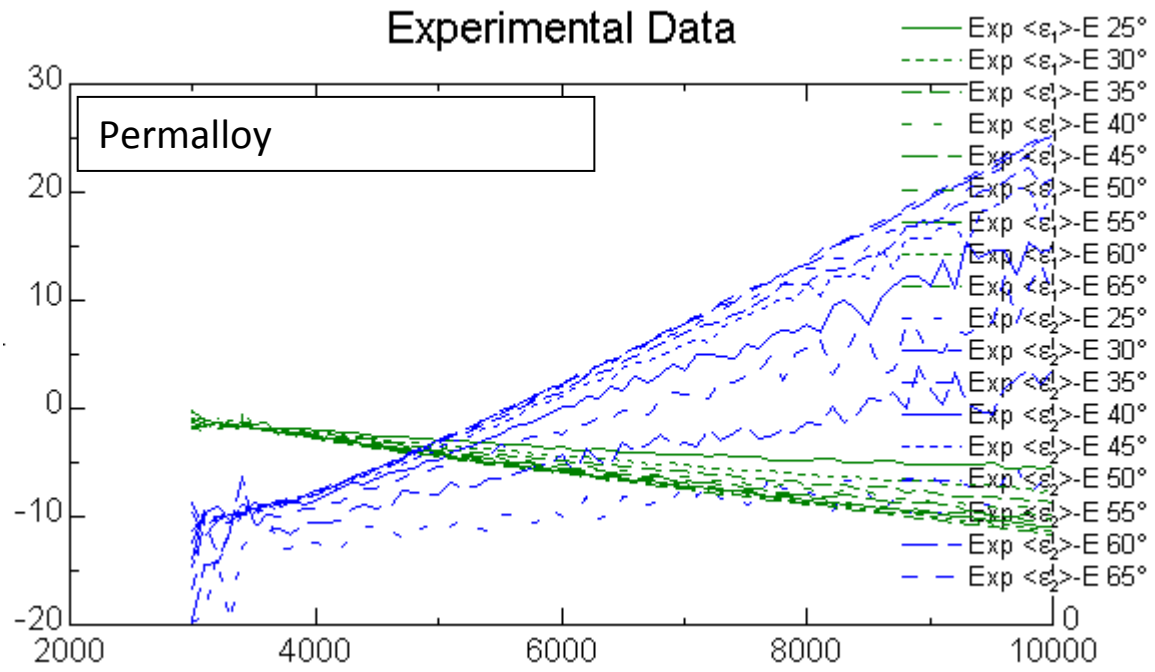

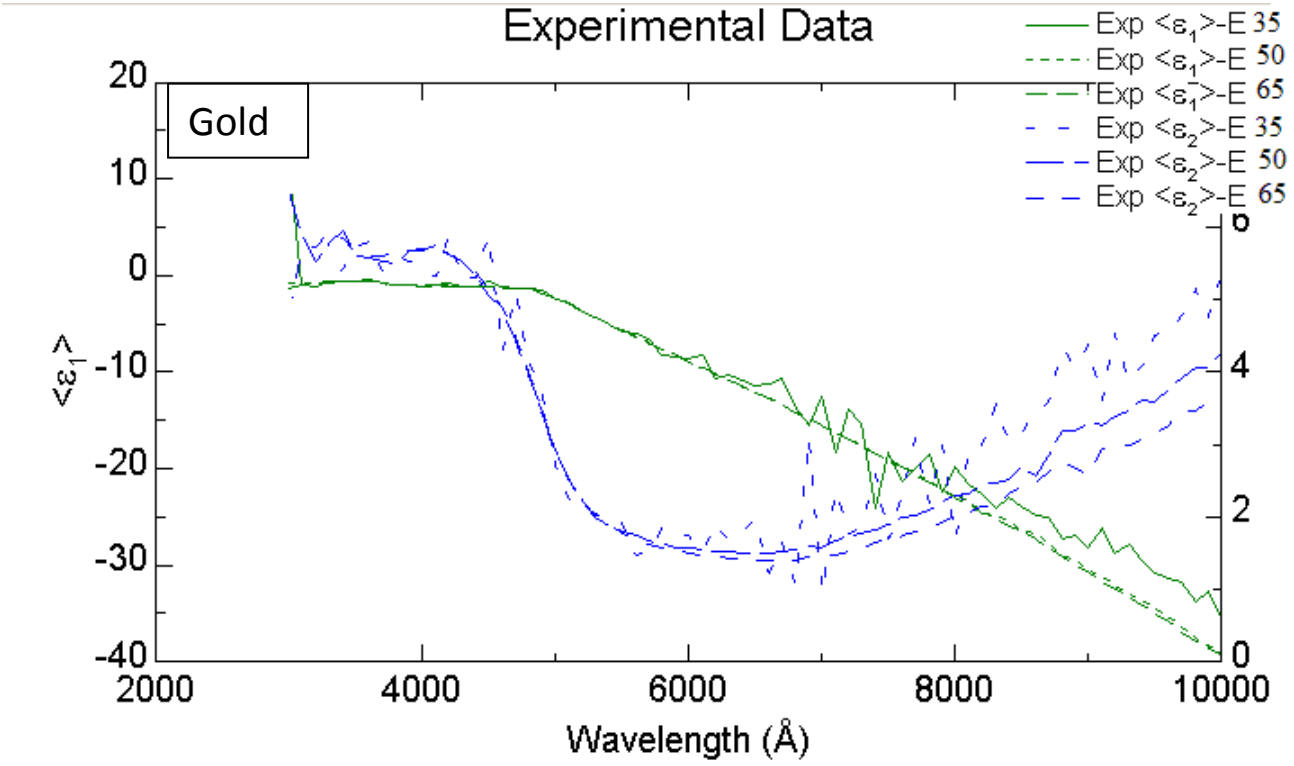

Plasmonic Excitations in Nanostructures

(Thesis for Bachelor of Science with Honours)

Summary of Student Achievements

In this project most of the experimental work and theoretical analysis has been done solely by myself. In detail, my personal achievements include:

1. Recommissioning and upgrading the vacuum chamber that has been used for deposition of metal films for optical studies;

2. Deposition of thin films using this chamber;

3. Conducting all the measurements on thin films and nanopatterned structures using optical spectroscopy techniques, namely ellipsometry and reflection spectroscopy;

4. Designing and implementing an upgrade to the ellipsometer in order to record the magnetic-field-resolved (MFR) spectra, in particular[1]:

- developement of a method to use the high sensitivity of polarisation measuring mode of the ellipsometer to detect the weak MOKE signals;
- design and fabrication of the electromagnet and of a holder to fix it to the ellipsometer;
- design and fabrication of the custom Digital-To-Analog converter box (schematics, pcb, soldering, etc.);
- development of software to control the measurement and to process the output MFR data;

5. Realizing that from the variety of magneto-optical phenomena the Transverse MOKE effect is the most suitable for observation on the nanostructures with the standard optical ellipsometry;

6. Processing and analysing the data acquired from the optical measurements, including:

- estimating thicknesses of films;
- deriving loss spectra from ellipsometry data;
- processing reflectivity data and plotting model fits;
- processing MFR ellipsometry data to obtain Transverse MOKE spectra.

As a result of the above work I have successfully observed the excitation of plasmons in thin films and nanostructured samples. I have also detected the enhancement of MOKE effect in the transverse configuration.

I have conducted most of the literature search (articles, books) and provided the theoretical explanations of the observed effects on the basis of these works, namely I suggested explanations for the effects:

- observed in rough films of silver;
- seen in Ag/W(110) SPEELS spectra;
- seen in gold, Permalloy, and Au/Permalloy nanostripes.

Recording of SPEELS spectra of Ag/W(110) have been conducted by my supervisor, Prof. S.Samarin. In this experiment I have been assisting him with deposition of films, upgrading and using the acquisition software, and taking measurements of LEEDS and AES.

Nikita Kostylev *November, 2, 2011*

[1] All designs and fabrications have been performed by myself without any assistance from Physics Workshop or other contractors

B.Sc. (Hons) Physics Project

Research Proposal

Nikita Kostylev
School of Physics, University of Western Australia

March 2011

Plasmon Excitations in Nanostructures

Keywords: surface plasmons, nanostructures, nanodot arrays, spectroscopy
Supervisors: W/Prof. James Williams (UWA), Prof. Sergey Samarin (UWA)

1 Research Plan

1.1 Aims

This project is set to investigate electronic properties of thin metal films and nanostructures. It involves preparation of systems that are capable of generating detectable plasmon oscillations. The samples to be tested will be based on metal/ferromagnetic metal multilayered structures created in Ultra-High Vacuum (UHV) conditions. They will include non-periodic (continuous) films, as well as periodic 'nanodot' arrays. Measurements will include such techniques as Total Current Spectroscopy (TCS), Electron Energy Loss Spectroscopy (EELS), Optical Spectroscopy and Ellipsometry.

1.2 Significance

Currently used silicon semiconductor systems based on electron current transmission are believed to be close to reaching their limit of scalability (Thompson et al., 2006) possibly resulting in a decrease of global technological progress rate. A viable solution to this problem involves replacing electrons in such devices with photons. Metal nanostructures, supporting collective electron oscillations - plasmons, act as optical nanoantennae by concentrating large electromagnetic energy in the nanoscale volume. Development of suitable plasmonic nanostructures, which can serve as optical couplers, connecting micro-sized components with nanoscaled optical systems (Bozhevolnyi et al., 2006), would allow significant progress in the area of nanophotonics and plasmonics.

1.3 Method

Surface plasmons are collective electronic excitations near the surfaces of metallic structures. The model to describe such excitations has been developed in the 1950s by Bohm and Pines (Pines, 1957). This theory treats the lattice electrons within a metal as a free degenerate electron gas, influenced by a field of isotropically distributed positive ion cores. The Bohm-Pines model has shown that besides classical Coulomb electron-electron interactions, long-range collective interactions will result in organised oscillations of electrons. The frequency of such oscillations in the simplest case can be found (Dobretsov et al., 1971) from:

$$\nu_p = \frac{1}{2\pi}\sqrt{\frac{4\pi n e^2}{m_e}}\,, \tag{1}$$

where n is the electron number density. The plasmon energies are given by $E_p = h\nu_p$. The plasmons in certain conditions can decay in an optical regime, emitting photons. Plasmon energies in different metals vary from about 3 to 30 eV (Dobretsov et al., 1971).

Electron Energy Loss Spectroscopy is one of the most efficient techniques to observe and study plasmon excitations in noble metals (Pulisciano et al., 2008). In this method, energies of electrons, inelastically scattered from a surface, are measured. In EELS experiments conducted on thin Ag films on W(100) substrate, the plasmons excited by low energy electrons were observed to decay with the emission of photons with energies corresponding to bulk and surface plasmons (Samarin et al., 1996). The relative contribution of these two maxima depended on film thickness (Samarin et al., 1996), temperature (Artamonov et al., 1981) and deposition of an additional material on top of the silver film (Artamonov et al., 1983).

In this Honours project, samples of thin-films of noble metals, such as Au and Ag, will be prepared by evaporative deposition in UHV conditions. A number of test films will be produced, with different substrates and thickness. They will be analysed using polarization measurements of reflected optical light (Ellipsometry) for the accurate estimation of physical parameters of samples, such as film thickness and optical characteristics. It will also provide us with some details of the electronic structure. Total Current Spectroscopy will be employed to control the surface potential and changes to the work-function of the surface. This will be done by measuring the sample current while varying the potential difference between the sample and the cathode. Finally, electron energy losses due to plasmon excitation will be measured in these films using EELS and results analysed. Nanodot samples will be also characterised using ellipsometry and possibly EELS. The goal will be to attempt detection of plasmonic oscillations in this confined geometry.

1.4 Status

Research projects directed at studying plasmon excitations in various structures have been undertaken over the recent years by numerous groups, mostly overseas (Artamonov et al., 1981; Pulisciano et al., 2008; Zamkovets et al., 2011). This research area remains rather underdeveloped here at UWA though, with very few experiments conducted. This project would allow establishing a base for future plasmonic and magneto-plasmonic studies at the Centre for Atomic, Molecular and Surface Physics (CAMSP).

At this time, the technological stage of the project is under development. A vacuum chamber has been assembled and high levels of vacuum (10^{-9} Torr) have been achieved. Currently, the optimal configuration of film deposition and spectroscopy equipment within the constraints of the chamber is being investigated. Also additional tests are being performed on chamber's gaskets, seals and internal surfaces, in order to minimize leaks and hence to reach even better vacuum conditions.

2 Benefits

General trends in electronic devices are miniaturization, high speed of operation and data transmission, while consuming extremely low power. Research undertaken within this project would allow development of new materials and techniques that explore the possibility of implementing optical devices of the nanometre size in electronics. Such systems promise higher processing and transmission speeds, while at the same time even further reducing the size of electronic components. Hence this technology would allow the trends currently observed in electronics to remain sustainable in the far future.

3 Publications

Research in the area of plasmonics is currently experiencing rapid growth. A lot of studies have been done in the field of plasmon and magneto-plasmon excitations in noble metal/ferromagnetic structures (Pulisciano et al., 2008; Temnov et al., 2010). One of the project supervisors has also extensively studied plasmon excitations in Ag films by low energy electrons (Artamonov et al., 1981, 1983; Samarin et al., 1996).

4 Costs

This project is largely of experimental nature. The main costs are associated with establishing appropriate UHV conditions. The total cost of the vacuum chamber parts, pumps, seals and other consumables are on the order of AUD20,000-30,000. Measurement and film deposition equipment cost is also significant, estimated to be around AUD150,000. Fortunately, most of the equipment is already available within CAMSP from previous projects and grants. A state-of-the-art optical spectrometer has been recently purchased. Unique nanodot film samples have also already been sourced from the group led by A/Prof. A. Adeyeye from the National University of Singapore.

References

Artamonov, OM, Samarin, SN, Dimakova, EB, Kuchma, AE & Yakovlev, II 1981, 'Temperature dependence of photon emission under irradiation of a thin silver film by slow electrons', Optics and Spectroscopy, vol. 50, no.5, pp. 911-15, USSR.

Artamonov, OM, Samarin, SN & Yakovlev, II 1983, 'Characteristics of low-voltage cathodoluminescence of BaO films on tungsten and silver', Optics and Spectroscopy, vol.54, no. 3, pp. 459-63, USSR.

Bozhevolnyi, SI & Shalaev, VM 2006, 'Nanophotonics with surface plasmons - Part I - The evolving field of nanophotonics seeks to combine the capabilities of nanotechnology and photonics', Photonics Spectra, vol. 40, no. 1, p. 58.

Dobretsov, LN & Gomoyunova, MV 1971, Emission Electronics, Keter Press, Jerusalem.

Pines, D 1957, Uspekhi Fizicheskih Nauk, vol. 62, p. 399.

Pulisciano, A, Park, SJ & Palmer, RE 2008, 'Surface plasmon excitation of Au and Ag in scanning probe energy loss spectroscopy', Applied Physics Letters, vol. 93, no. 21.

Samarin, SN & Yakovlev, II 1996, Notions and Perspectives of Nonlinear Optics, World Scientific, pp. 518-524, Singapore.

Temnov, VV, Armelles, G, Woggon, U, Guzatov, D, Cebollada, A, Garcia-Martin, A, Garcia-Martin, JM, Thomay, T, Leitenstorfer, A & Bratschitsch, R 2010, 'Active magneto-plasmonics in hybrid metal-ferromagnet structures', Nature Photonics, vol. 4, no. 2, pp. 107-111.

Thompson, SE & Parthasarathy, S 2006, 'Moore's law: the future of Si microelectronics', Materials Today, vol. 9, no. 6, pp. 20-25.

Zamkovets, AD, Ponyavina, AN, Aksimentyeva, OI & Baran, LV 2011, 'Surface Plasmon Resonance in Nanostructures Based on Polyparaphenylene - Silver Monolayers', Molecular Crystals and Liquid Crystals, vol. 536, pp. 86-92.